

# A local level set method for three-dimensional inversion of gravity gradient data

Wangtao Lu<sup>1</sup> and Jianliang Qian<sup>2</sup>

<sup>1</sup> *Department of Mathematics, Michigan State University, East Lansing, MI 48824. Email:*

**wangtaol@math.msu.edu**

<sup>2</sup> *Department of Mathematics, Michigan State University, East Lansing, MI 48824. Email:*

**qian@math.msu.edu**

(September 6, 2014)

Running head: **Level-set inversion of gravity gradient data**

## ABSTRACT

We propose a local level set method for inverting 3-D gravity gradient data. To alleviate inherent non-uniqueness of the inverse gradiometry problem, we assume that a homogeneous density contrast distribution with the value of density contrast specified a priori is supported on an unknown bounded domain  $D$  so that we may convert the original inverse problem into a domain inverse problem. Since the unknown domain  $D$  may take a variety of shapes, we parametrize the domain  $D$  by a level-set function implicitly so that the domain inverse problem is reduced to a nonlinear optimization problem for the level-set function. Since the convergence of the level-set algorithm relies heavily on initializing the level-set function to enclose the gravity center of a source body, we apply a weighted  $L^1$ -regularization method to locate such a gravity center so that the level-set function can be properly initialized. To compute rapidly the gradient of the nonlinear functional arising in the level-set formulation, we make use of the fact that the Laplacian kernel in the gravity force relation decays rapidly off the diagonal so that matrix-vector multiplications for evaluating the gradient can be accelerated significantly. Extensively numerical experiments demonstrate performance and effectiveness of the new method.

## INTRODUCTION

Gravity gradiometer measures the gravity gradient tensor, consisting of the gradient of each component of the gravity field, at or above the ground surface of the earth. Modern gradiometry instruments, such as the FTG system and the Airborne FALCON system, measure (directly or indirectly) the differential curvature and the gradient of the vertical component of the gradient of the potential field (Pilkington, 2012) as the gravity gradient tensor only contains five independent components. Interpretation of gravity gradient data is one of the most significant tasks in geological sciences since such interpretation can help to analyze the composition of the earth and target subsurface source bodies, such as mineral deposits and so on. Since recently developed airborne systems can collect the gravity-related data in much larger areas more quickly and cheaply than traditional ground-based systems, and since the gravity gradient data are more sensitive to lateral variability of sub-surface source bodies and hence can perhaps provide better lateral resolution than gravity data, gravity gradient data have become more attractive in practical surveys nowadays. However, since gravity gradient data are higher order derivatives of the potential, manual interpretation of such data is extremely challenging while automatic interpretation calls for developing efficient inversion methods.

Many techniques (Last and Kubik, 1983; Li and Oldenburg, 1998; Portniaguine and Zhdanov, 1999; Condi and Talwani, 1999; Jorgensen and Kisabeth, 2000; Li, 2001b,a; Routh et al., 2001; Zhdanov et al., 2004; Krahenbuhl and Li, 2006; Barnes et al., 2008; Li, 2010; Martinez et al., 2010; Barnes and Barraud, 2012; Martinez et al., 2013) have been developed for the inversion of gravity data or gravity gradient data during the last decades; prior geological information and constraints on density models are usually incorporated in the existing techniques to ensure that the resulting solutions conform to realistic earth models (Last and Kubik, 1983; Li and Oldenburg, 1998; Condi and Talwani, 1999; Portniaguine and Zhdanov, 1999). Meanwhile, fast imaging methods (Fedi and Florio, 2006; Fedi, 2007; Zhdanov et al., 2011; Cella and Fedi, 2012; Fedi and Pilkington, 2012) have also been developed to directly locate the gravity center of a source body. Since most

inversion techniques provide quantitative descriptions for subsurface structures, one has to extract the position of a source body from resulting solutions afterwards, and this is not an easy task. Therefore, to avoid such indirect extracting procedure, we are motivated to develop a more direct method to delineate subsurface source bodies.

We propose for inverting 3-D gravity gradient data a local level set method, which automatically determines positions of source bodies. The method is analogous to a recently developed local level set method for the inversion of gravity data (Isakov et al., 2011, 2013; Lu et al., 2014). Mathematically, we formulate the inversion of gravity gradient data as the following inverse problem: find the density contrast  $\rho$  in a subsurface domain  $\Omega$ , given gravity gradient data on a measurement surface  $\Gamma \subset \mathbb{R}^3/\Omega$ . To alleviate inherent non-uniqueness of the inverse gradiometry problem, we assume that a homogeneous density contrast  $\rho$  is supported on an unknown bounded domain  $D$  of constant density contrast  $\rho_0$ , that is,  $\rho = \rho_0\chi_D$ , so that we may convert the original inverse problem into a domain inverse problem. Although subsurface source bodies can have arbitrary density distributions, by the equivalent-source principle, there exists an average density contrast  $\rho_0$  and an associated domain  $D$  so that the density distribution  $\rho = \rho_0\chi_D$  can reproduce the given gradiometry data. However, one cannot find the value of density contrast  $\rho_0$  and the domain  $D$  simultaneously since there may exist infinitely many pairs  $\{\rho_0, D\}$  that will reproduce the same gradiometry data. Fortunately, since prior information on subsurface structures can help to determine  $\rho_0$ , we only need to find the domain  $D$ .

Since the unknown domain  $D$  may have a variety of possible shapes, we introduce a level set function to parametrize the domain  $D$  so that the domain inverse problem is reduced to a nonlinear optimization problem for the level set function. Since the convergence of the level-set algorithm relies heavily on initializing the level-set function to enclose the gravity center of a source, we apply a weighted  $L^1$ -regularization method to locate such a gravity center so that the level-set function can be properly initialized. To compute rapidly the gradient of the nonlinear functional arising in the level-set formulation, we make use of the fact that the Laplacian kernel in the gravity force relation decays rapidly off the diagonal so that matrix-vector multiplications for evaluating the

gradient can be accelerated significantly.

The reason that we choose the level-set method for the inverse gradiometry problem is the following. For the geometrical domain inverse problem under consideration, one needs to deal with closed irregular surfaces which are the boundary of an underlying domain. To describe such an irregular surface, one may introduce some surface parametrization so that one can carry out manipulation on such a surface in order to fit the given data. However, because such an irregular surface may change shapes or connectivities during nonlinear data-fitting process, we need to design a reliable and robust parameterization which is capable of changing shapes or connectivities automatically, and the level-set implicit parametrization (Osher and Sethian, 1988) is exactly such a parametrization. We start with a continuous function which is defined everywhere in the whole computational domain, and we further require that this function be positive inside a targeted domain and negative outside, which implies that the zero level-set where the function is zero describes exactly the boundary of the targeted domain, and this function is called the level-set function. A level-set implicit parametrization gives rise to many advantages, such as we have a globally defined functions to manipulate, and the changes of geometry shape and connectivities can be automatically taken care of due to the underlying physical mechanism.

We remark that in the literature the level-set method (Osher and Sethian, 1988) has been widely used as a suitable and powerful tool for interfaces and shape-optimization problems mainly due to its ability in automatic interface merging and topological changes. In terms of non-geophysical inverse problems, the level-set method was first used for inverse obstacle problems in Santosa (1996); since then it has been applied to a variety of inverse problems. In Litman et al. (1998) it was used to reconstruct 2-D binary obstacles; in Burger (2001) different choices of descent directions to evolve level-sets were proposed for inverse obstacle problems; furthermore, the level-set method was used for inverse scattering problems to reconstruct geometry of extended targets in Hou et al. (2004) and Dorn and Lesselier (2006), for electrical resistance tomography in medical imaging in Ben Hadj Miled and Miller (2007), and for piece-wise constant surface reconstruction in van den Doel et al. (2010); see Burger and Osher (2005) for a survey of related applications. In terms of

geophysical inverse problems, the level-set method has also found its wide applications, and the following citations are by no means complete. In Isakov et al. (2011), the level-set method was first applied to the gravity data; in Papadopoulos et al. (2011) it was applied to identify uncertainties in the shape of geophysical objects using temperature measurements; in Zheglova et al. (2013), Li and Leung (2013) and Li et al. (2014) it was applied to travel-time tomography problems in different settings.

The rest of this paper is organized as follows. We start to present the methodology by developing a level-set-based formulation for the inverse gradiometry problem and then address several implementation issues. Numerical experiments are carried out to exhibit performance and effectiveness of the local level set method.

## METHODOLOGY

### Inverse gradiometry problem

We begin with the mathematical description of the inverse gradiometry problem. The gravity potential field  $u$  satisfies:

$$u(\mathbf{r}; \rho) = 4\pi\gamma \int_{\Omega} K(\mathbf{r}, \tilde{\mathbf{r}}) \rho(\tilde{\mathbf{r}}) d\tilde{\mathbf{r}}, \quad \mathbf{r} \in \Gamma, \quad (1)$$

where  $\Omega \in \mathbb{R}^3$  is a subsurface domain,  $\rho$  is the density in  $\Omega$ ,  $K$  is Green's function of the 3-D Laplace equation,

$$K(\mathbf{r}, \tilde{\mathbf{r}}) = \frac{1}{4\pi|\mathbf{r} - \tilde{\mathbf{r}}|}, \quad \mathbf{r} \neq \tilde{\mathbf{r}},$$

$\gamma$  is the universal gravitational constant,  $\Gamma \subset \mathbb{R}^3/\Omega$  is the measurement surface,  $\mathbf{r} = (x, y, z)$  and  $\{x, y, z\}$  is the standard Cartesian coordinate system.

Gravity gradiometer measures the gradient of each component of the gravity field on  $\Gamma$ , com-

prising the following gravity gradient tensor:

$$\mathbf{T} = \begin{bmatrix} u_{xx} & u_{xy} & u_{xz} \\ u_{yx} & u_{yy} & u_{yz} \\ u_{zx} & u_{zy} & u_{zz} \end{bmatrix}. \quad (2)$$

Since  $u$  satisfies the Laplace equation outside  $\Omega$  and the differential operators are commutative, the gravity tensor  $\mathbf{T}$  is symmetric with a zero trace and only five components in  $\mathbf{T}$  are linearly independent. Modern gradiometers measure some or all of the following five components: the differential curvature components, namely  $u_{xy}$  and  $u_{\Delta} = (u_{xx} - u_{yy})/2$ , and the gradient of the vertical gravity field, namely  $u_{zz}$ ,  $u_{xz}$  and  $u_{yz}$ . In fact, we have

$$u_s(\mathbf{r}; \rho) = 4\pi\gamma \int_{\Omega} K_s(\mathbf{r}, \tilde{\mathbf{r}}) \rho(\tilde{\mathbf{r}}) d\tilde{\mathbf{r}}, \quad \mathbf{r} \in \Gamma, \quad (3)$$

for any  $s \in \mathbf{M}_{all} = \{\Delta, xy, zz, xz, yz\}$ . Here  $K_s$  denotes the second order partial derivative of Green's function  $K$  with respect to the component indexed by  $s$ ; in particular,

$$K_{\Delta} = \frac{1}{2}(\partial_x^2 K - \partial_y^2 K).$$

Normally, we always separate the residual gravity field from the remaining background field so that we only need to analyze the distribution of the density contrast over the remaining background; without confusing, we will overload  $u$  and  $\rho$  as the residual gravity potential on  $\Gamma$  and the density contrast in  $\Omega$ , respectively, and we will refer to the residual gravity field as the gravity field in the following. Thus, mathematically, we can formulate the inverse gradiometry problem as follows: find the density contrast  $\rho$  in a subsurface domain  $\Omega$ , given the gravity gradient data on the measurement surface  $\Gamma \subset \mathbb{R}^3/\Omega$ . To alleviate inherent non-uniqueness of the inverse gradiometry problem, we assume that the homogeneous density contrast  $\rho$  in  $\Omega$  is supported on an unknown bounded domain  $D \subset \Omega$ , i.e.,  $\rho = \rho_0 \chi_D$ , where  $\rho_0$  is a constant. As  $\rho_0$  and  $D$  cannot be determined

simultaneously, we assume that the density contrast  $\rho_0$  is known in advance. Therefore, the inverse gradiometry problem can be restated as: find the unknown domain  $D \subset \Omega$  with a given density contrast  $\rho_0$  that satisfies the following condition

$$u_s(\mathbf{r}; \rho_0 \chi_D) = g_s(\mathbf{r}), \quad \text{for } \mathbf{r} \in \Gamma, \quad (4)$$

for  $s$  belonging to an index set  $\mathbf{M} \subset \mathbf{M}_{all}$ , where  $\{g_s\}_{s \in \mathbf{M}}$  are the set of gradient data measured on the surface  $\Gamma \subset \mathbb{R}^3/\Omega$ .

### A level-set-based formulation

As  $D$  may have a variety of possible shapes or connectivities, we propose to parametrize its boundary by a level set function  $\phi^* : \Omega \rightarrow \mathbb{R}$ , which is continuous and satisfies

$$\phi^*(\mathbf{r}) > 0, \quad \text{for } \mathbf{r} \in D, \quad (5a)$$

$$\phi^*(\mathbf{r}) = 0, \quad \text{for } \mathbf{r} \in \partial D, \quad (5b)$$

$$\phi^*(\mathbf{r}) < 0, \quad \text{for } \mathbf{r} \in \bar{D}^c. \quad (5c)$$

Thus, we have for  $s \in \mathbf{M}$ ,

$$g_s(\mathbf{r}) = u_s(\mathbf{r}; \rho_0 \chi_D) = 4\pi\gamma\rho_0 \int_D K_s(\mathbf{r}, \tilde{\mathbf{r}}) d\tilde{\mathbf{r}} = 4\pi\gamma\rho_0 \int_\Omega K_s(\mathbf{r}, \tilde{\mathbf{r}}) H(\phi^*(\tilde{\mathbf{r}})) d\tilde{\mathbf{r}}, \quad (6)$$

where  $H$  is the Heaviside function defined by

$$H(x) := \begin{cases} 1, & x \geq 0, \\ 0, & \text{otherwise.} \end{cases}$$

For any level set function  $\phi : \Omega \rightarrow \mathbb{R}$ , we define the forward operator  $\mathbf{A}$  as:

$$\mathbf{A}(\phi) = [A_s(\phi)]_{s \in \mathbf{M}}, \quad (7)$$

$$A_s(\phi)(\mathbf{r}) = 4\pi\gamma\rho_0 \int_{\Omega} K_s(\mathbf{r}, \tilde{\mathbf{r}}) H(\phi(\tilde{\mathbf{r}})) d\tilde{\mathbf{r}}, \quad (8)$$

where  $[A_s]_{s \in \mathbf{M}}$  denotes a column vector of  $A_s$  for  $s \in \mathbf{M}$ .

We solve the following minimizing problem to find  $\phi^*$ :

$$\min J(\phi) = \min \|\mathbf{A}(\phi) - \mathbf{g}\| = \min \sum_{s \in \mathbf{M}} \|G_s(\cdot; \phi)\|_{L^2(\Gamma)}^2, \quad (9)$$

where  $\mathbf{g} = [g_s]_{s \in \mathbf{M}}$  and the mismatch term

$$G_s(\mathbf{r}; \phi) = A_s(\phi)(\mathbf{r}) - g_s(\mathbf{r}), \quad (10)$$

for  $s \in \mathbf{M}$ . According to equation (6),  $J(\phi)$  attains the minimum at  $\phi = \phi^*$ .

A necessary condition for  $\phi$  being a minimizer is that the Frechet derivative of the objective functional  $J$  with respect to  $\phi$  is 0. The Frechet derivative  $\partial J / \partial \phi$  is well-defined through

$$J(\phi + h) - J(\phi) = \left\langle \frac{\partial J}{\partial \phi}, h \right\rangle + o(\|h\|) \quad (11)$$

for any  $h \in L^2(\Omega)$ , where  $\langle \cdot, \cdot \rangle$  is the standard inner product in  $L^2(\Omega)$ .

Since

$$\begin{aligned}
J(\phi + h) - J(\phi) &= \sum_{s \in \mathcal{M}} \int_{\Gamma} [G_s(\mathbf{r}; \phi + h)^2 - G_s(\mathbf{r}; \phi)^2] d\sigma(\mathbf{r}) \\
&= 4\pi\gamma\rho_0 \sum_{s \in \mathcal{M}} \int_{\Gamma} \left\{ (2G_s(\mathbf{r}; \phi) + o(\|h\|)) \int_{\Omega} K_s(\mathbf{r}, \tilde{\mathbf{r}}) [H(\phi + h) - H(\phi)] d\tilde{\mathbf{r}} \right\} d\sigma(\mathbf{r}) \\
&= 4\pi\gamma\rho_0 \sum_{s \in \mathcal{M}} \int_{\Gamma} \left\{ 2G_s(\mathbf{r}; \phi) \int_{\Omega} K_s(\mathbf{r}, \tilde{\mathbf{r}}) [\delta(\phi(\tilde{\mathbf{r}}))h(\tilde{\mathbf{r}}) + o(\|h\|)] d\tilde{\mathbf{r}} \right\} d\sigma(\mathbf{r}) + o(\|h\|) \\
&= \sum_{s \in \mathcal{M}} \int_{\Omega} \left\{ h(\tilde{\mathbf{r}}) 8\pi\gamma\rho_0 \int_{\Gamma} G_s(\mathbf{r}; \phi) K_s(\mathbf{r}, \tilde{\mathbf{r}}) d\sigma(\mathbf{r}) \delta(\phi(\tilde{\mathbf{r}})) \right\} d\tilde{\mathbf{r}} + o(\|h\|),
\end{aligned}$$

we obtain

$$\frac{\partial J}{\partial \phi}(\tilde{\mathbf{r}}) = 8\pi\gamma\rho_0 \sum_{s \in \mathcal{M}} \int_{\Gamma} G_s(\mathbf{r}; \phi) K_s(\mathbf{r}, \tilde{\mathbf{r}}) d\sigma(\mathbf{r}) \delta(\phi(\tilde{\mathbf{r}})). \quad (12)$$

Therefore, the necessary condition is simplified to

$$0 = \frac{\partial J}{\partial \phi} = 8\pi\gamma\rho_0 \sum_{s \in \mathcal{M}} \int_{\Gamma} G_s(\mathbf{r}; \phi)^T K_s(\mathbf{r}, \tilde{\mathbf{r}}) d\sigma(\mathbf{r}) \delta(\phi(\tilde{\mathbf{r}})), \quad (13a)$$

$$0 = \frac{1}{|\nabla \phi|} \frac{\partial \phi}{\partial \boldsymbol{\nu}} \quad \text{on} \quad \partial\Omega, \quad (13b)$$

where  $\boldsymbol{\nu}$  denotes the unit normal vector to  $\partial\Omega$  and we impose the natural boundary condition on  $\phi$  so that  $\phi$  does not change rapidly away from  $\Omega$ . By the method of steepest descent, we end up with the evolution equation

$$\frac{\partial \phi}{\partial t} = -\frac{\partial J}{\partial \phi}, \quad (14a)$$

$$0 = \frac{1}{|\nabla \phi|} \frac{\partial \phi}{\partial \boldsymbol{\nu}} \quad \text{on} \quad \partial\Omega, \quad (14b)$$

where  $\phi = \phi(\mathbf{r}, t)$  with  $t$  being the artificial evolution time. Therefore, we take the exact solution to be  $\phi^* = \phi(\mathbf{r}, \infty)$  and the boundary  $\partial D$  to be the zero level set of  $\phi^*$ :  $\partial D = \{\mathbf{r} : \phi^*(\mathbf{r}) = 0\}$ .

We remark that our level-set-based formulation provides implicit regularization in the evolution process. More specifically, to ensure that the evolution equation guides the level set function  $\phi$

towards the exact solution  $\phi^*$  stably, we need to reinitialize the level set function  $\phi$  frequently, so that  $|\nabla\phi| = 1$  in  $\Omega$  and the level set function  $\phi$  does not change rapidly near interfaces (Sussman et al., 1994); this reinitialization procedure serves as an implicit regularization on the inverse gradiometry problem. Next, the evolution equation requires that the level set function  $\phi$  be at least differentiable once, which is considered to be another implicit regularization. In addition, the coarseness of discretization of  $\Omega$  can be considered to be an implicit regularization as well since it may affect the resolution of numerical inversions.

In the following, we take the computational domain  $\Omega$  to be a rectangular cuboid and the measurement surface  $\Gamma$  to be a planar surface above the top face of  $\Omega$ .

## Numerical implementation

We apply the following level-set algorithm to find  $D$ :

**Algorithm 1**    0. Choose an index set  $\mathbf{M} \in \mathbf{M}_{all}$  and a density contrast  $\rho_0$  according to prior information.

1. Initialize the level set function  $\phi$  according to the index set  $\mathbf{M}$  obtained in Step 0.
2. Compute the mismatch  $G_s(\mathbf{r})$  along the boundary  $\Gamma$  according to (10) for each  $s \in \mathbf{M}$ .
3. Compute the Frechet derivative in (12).
4. Evolve the level set function according to the gradient flow (14).
5. Reinitialize the level set function to maintain the signed distance property.
6. Repeat 2-5 until it converges.

In the following, we give motivations and details on implementing each step of the above algorithm.

*Step 0: the index set  $\mathbf{M}$  and the density contrast  $\rho_0$*

In practice, any data type with the index set  $\mathbf{M}$  being a subset of  $\mathbf{M}_{all}$  can be used in an inversion as all five independent components  $\{u_s\}_{s \in \mathbf{M}_{all}}$  can be measured by common gradiometers, such as the full tensor gravity (FTG) system and the Falcon system; the FTG instrument measures all five independent components directly, and the Falcon instrument measures  $u_{xy}$  and  $u_{\Delta}$  only, from which the other three components  $u_{xz}$ ,  $u_{yz}$  and  $u_{zz}$  are derived in order to minimize the high noise levels from vertical accelerations (Lee, 2010; Pilkington, 2012). For example, Li (2001b) developed an inversion method for all five independent components whereas Li (2010) used  $u_{xy}$  and  $u_{\Delta}$  only. However, a number of works have shown that not all the five independent components are needed in illuminating source bodies.

Condi and Talwani (1999) found that  $u_{xy}$  and  $u_{\Delta}$  can produce as accurate result as all the five components together do. Zhdanov et al. (2004) suggested that using  $u_{xy}$  and  $u_{\Delta}$  together can produce better results than  $u_{zz}$  alone whereas Fullagar and Pears (2010) suggested that using  $u_{zz}$  alone is the best choice and that inversion of multiple components adds little when  $u_{zz}$  is available. Martinez et al. (2010) and Martinez et al. (2013) compared  $u_{zz}$ , a combination of  $u_{xz}$ ,  $u_{yz}$  and  $u_{zz}$ , and a full-tensor-element combination, and showed that  $u_{zz}$  is sufficient to produce geologically reasonable and interpret-able results and that including additional components increases resolution. Pilkington (2012) investigated the information content provided by each of the tensor components and combinations thereof by using ideas from optimal survey design and concluded that at smaller measurement-source distances  $u_{zz}$  shows the best performance while at larger measurement-source distances  $u_{xy}$ ,  $u_{\Delta}$ , and  $u_{xy}$  combined with  $u_{\Delta}$  are the best performers. Since most publications suggest the use of components from  $u_{zz}$ ,  $u_{xy}$  and  $u_{\Delta}$ , we will consider mainly three cases in the following numerical examples: (1)  $\mathbf{M} = \{xy, \Delta\}$ ; (2)  $\mathbf{M} = \{zz\}$ ; (3)  $\mathbf{M} = \{xy, \Delta, zz\}$ .

Although subsurface source bodies may have arbitrary density contrast distributions, usually a range of density contrasts of subsurface source bodies can be determined from prior information; we suggest to assign  $\rho_0$  any value from that range in that the level-set formulation requires that

the density contrast of subsurface source bodies be of the same value. This is reasonable when the minimum and maximum of the range are not far away from each other. For example, if the range of subsurface density contrast distribution is from  $0.8\text{g/cm}^3$  to  $1\text{g/cm}^3$ , any constant  $\rho_0$  in this range leads to at most 25% over-estimate of volume of some source body or 20% under-estimate of that, which is acceptable in practice.

*Step 1: initialization of level-set function*

Since there exist infinitely many pairs  $\{\rho_0, D\}$  of density models that can produce the same measurement data, it is impossible to determine  $\rho_0$  and  $D$  simultaneously. However, we expect that there may exist some intrinsic property of the domain  $D$  that is independent of  $\rho_0$ , and we expect that this intrinsic property may be beneficial to initialize the level set function in Algorithm 1.

Motivated by this, we illustrate the relation between  $\rho_0$  and  $D$  by studying a simple example, the point-source model as shown in Figure 1(a). Let the computational domain  $\Omega$  be the cuboid  $[0, 1]\text{km} \times [1, 2]\text{km} \times [-0.4, 0]\text{km}$  and the measurement surface  $\Gamma$  be  $[0, 1]\text{km} \times [1, 2]\text{km} \times \{z = 0.1\text{km}\}$ . Assume that the density contrast distribution is a point source of mass  $1\text{E}/\gamma$  at  $\mathbf{r}_s = (0.5, 1.5, -0.15)^T\text{km}$ , i.e.,  $\rho(\mathbf{r}) = 1\text{E} \times \delta(\mathbf{r} - \mathbf{r}_s)/\gamma$ , where the unit  $\text{E} = 10^{-9}\text{s}^{-2}$ . We collect the differential curvature data,  $g_{xy}$  and  $g_{\Delta}$ , and the vertical gradient data,  $g_{zz}$  at  $33 \times 17 = 561$  mesh points which are uniformly distributed on  $\Gamma = [0, 1]\text{km} \times [1, 2]\text{km} \times \{z = 0.1\text{km}\}$  in both  $x$ - and  $y$ -directions. Patterns of data  $\{g_s\}_{s \in \{xy, \Delta, zz\}}$  are shown in Figure 1 (b-d).

Next, we try to determine the unknown domain  $D$  from two groups of data set,  $\{g_{xy}, g_{\Delta}\}$  and  $\{g_{zz}\}$ , for different values of  $\rho_0$  by the level set method, and try to find the desired property from resulting solutions.

In the implementation, we uniformly discretize the computational domain  $\Omega = [0, 1]\text{km} \times [1, 2]\text{km} \times [-0.4, 0]\text{km}$  into  $41 \times 41 \times 17 = 28577$  mesh points with grid size  $0.25\text{km}$  in each direction. Suppose

$$\rho_0 = 1\text{E}/\gamma/(4/3\pi(R/\text{km})^3),$$

where we consider three different cases: (a):  $R = 0.13\text{km}$ , (b):  $R = 0.1\text{km}$  and (c):  $R = 0.08\text{km}$ . We determine the unknown domain  $D$  for the three cases by Algorithm 1, where we initialize the level set function to be

$$\phi_0 = 0.1 - \|\mathbf{r} - \mathbf{C}\|,$$

a sphere centered at  $\mathbf{C} = (0.5, 1.5, -0.2)\text{km}$ . In fact, by Newton’s shell theorem, the unknown domain  $D$  is exactly the sphere centered at  $\mathbf{r}_s$  with radius  $R$  when the density contrast  $\rho_0 = 1\text{E}/\gamma/(4/3\pi(R/\text{km})^3)$ , as plotted in Figures 2(a, d, g), since this spherical source body and the point source have the same gravity center  $\mathbf{r}_s$  and the same mass. For comparison, numerical solutions for inverting differential curvature data-set  $\{g_{xy}, g_{\Delta}\}$  for different values of  $R$  are plotted in Figures 2(a, c, e) while those for vertical gradient data-set  $\{g_{zz}\}$  are plotted in Figures 2(b, d, f).

We make the following observations on Figures 2: each numerical solution matches with the relevant exact solution very well for each case, and for either data-set, the three numerical solutions with different density contrasts  $\rho_0$  have the same gravity center  $\mathbf{r}_s$  and seem to shrink to the gravity center  $\mathbf{r}_s$  as  $\rho_0$  increases. In other words, we have numerically verified Newton’s shell theorem by the local level set method and have found the following intrinsic property: numerical solutions for different values of  $\rho_0$  have the same gravity center. We believe that this property remains valid in general, and we may use this property to initialize the level-set algorithm. Specifically, if we can find the gravity center of each source body, then we consider a level set function representing a number of well-separated balls centered at those gravity centers to be a good initial level set function, since at least, this initial density model has the same gravity centers with the true model. Therefore, we are motivated to find the gravity centers to initialize the level-set algorithm.

To this end, we can employ existing non-iterative fast imaging methods, such as the DEXP method (Fedi, 2007), the migration method (Zhdanov et al., 2011), and so on. However, Fedi and Pilkington (2012) and Cella and Fedi (2012) have found that a physically dependent depth-weighting function should be chosen in those depth-weighting-based imaging methods; otherwise,

these methods may locate sources at incorrect depths. Nevertheless, our level-set-based inversion does not depend on depth-weighting functions so that it is still reasonable to use imaging methods with physically independent weighting functions for locating sources and gravity centers in terms of initializing the level-set algorithm. Thus, we apply the migration method (Zhdanov et al., 2011) to recover rough source locations. We will see from numerical results that an initial level-set function, with inaccurate depths or even inconsistent number of source bodies, can still be evolved to a reasonable solution matching with true models.

In some cases when subsurface source bodies are not well-separated, the aforementioned fast imaging methods may lose effectiveness (Fedi and Pilkington, 2012; Cella and Fedi, 2012). In this situation, we propose to use the following iterative  $L^1$ -regularization method so that subsurface source bodies may be resolved more easily.

In the context of inverse gradiometry problem, since the density contrast distribution  $\rho$  is assumed to have a compact support in  $\Omega$ , we look for a density contrast distribution  $\rho$  with compact support in  $\Omega$  so that extrema among the non-zeros may exhibit positions of the gravity centers. Since the  $L^1$ -norm based regularization promotes compact support (Brezis, 1974; Ozolins et al., 2013), we propose to solve for the desired density distribution the following nonlinear optimization problem:

$$\min_{\rho} \tilde{F}(\rho) := \min_{\rho} \left\{ \sum_{s \in \mathcal{M}} \left\| 4\pi\gamma \int_{\Omega} K_s(\cdot, \tilde{\mathbf{r}}) \rho(\tilde{\mathbf{r}}) d\tilde{\mathbf{r}} - g_s(\cdot) \right\|_{L^2(\Gamma)}^2 + \lambda \|W\rho\|_{L^1(\Omega)} \right\},$$

where  $\lambda > 0$  is the penalty parameter. Here, the depth-weighting function  $W$  is chosen according to Li and Oldenburg (1998); Li (2001b) as

$$W(\tilde{\mathbf{r}}) = d(\tilde{\mathbf{r}}, \Gamma)^{-\beta/2}$$

for  $\beta = 2$  with  $d(\tilde{\mathbf{r}}, \Gamma)$  being the depth of  $\tilde{\mathbf{r}}$  below the planar surface  $\Gamma$ .

Assuming that  $\Omega$  is discretized by  $N$  points and that there are  $M$  observation points on  $\Gamma$ , we

apply trapezoidal quadrature rules to discretize the relevant integrals in the above optimization problem and we end up with the following finite-dimensional optimization problem in matrix form:

$$\min_{\boldsymbol{\rho}} \tilde{F}(\boldsymbol{\rho}) := \min_{\boldsymbol{\rho}} \{ \|\mathbf{K}\boldsymbol{\rho} - \mathbf{b}\|_2^2 + \lambda \|\mathbf{W}\boldsymbol{\rho}\|_1 \}, \quad (15)$$

where  $\boldsymbol{\rho} \in \mathbb{R}^{N \times 1}$  represents the unknown density  $\rho$  at the  $N$  mesh points in  $\Omega$ ,  $\mathbf{b} \in \mathbb{R}^{M \times 1}$  represents measurement data  $g_s$  at the  $M$  observation points for all  $s \in \mathbf{M}$ , matrix  $\mathbf{K} \in \mathbb{R}^{M \times N}$  and the diagonal matrix  $\mathbf{W} \in \mathbb{R}^{N \times N}$  are related to the kernel and weighting functions  $K_s$  and  $W$ , respectively, and  $\|\cdot\|_l$  represents the  $l$ -norm for  $l = 1, 2$ . We apply the `l1_ls` package (Koh et al., 2007) to solve this nonlinear minimization problem (15). In our implementation, the  $L^1$  regularization solution of Problem (15) is computed on very coarse meshes as rough locations of gravity centers are adequate for our level-set algorithm.

*Steps 2 and 3: computing the mismatch functional and the Frechet derivative*

To compute the mismatch functional, one may adopt the wavelet compression (Li and Oldenburg, 2003) and the finite-difference forward solver (Farquharson and Mosher, 2009). Since the kernel matrix  $K_s(\mathbf{r}, \tilde{\mathbf{r}})$  in Eq. (3) decays rapidly as the distance  $|\mathbf{r} - \tilde{\mathbf{r}}|$  increases, the low-rank-matrix decomposition algorithm proposed in Lu et al. (2014) can be employed to speed up matrix-vector multiplications arising in computing the mismatch and the Frechet derivative. To avoid numerical instabilities (Zhao et al., 1996), the delta function  $\delta(\phi)$  in equation (13) is approximated by  $\delta_\epsilon(\phi) = \chi_{T_\epsilon} |\nabla \phi|$ , with support  $T_\epsilon = \{\mathbf{p} \in \Omega : |\phi(\mathbf{p})| \leq \epsilon\} \subset\subset \Omega$  for some  $\epsilon > 0$ .

To illustrate the performance of this low-rank-matrix decomposition algorithm, as listed in Table 1 we record running times for computing the Frechet derivative, with the index set  $\mathbf{M} = \{xy, \Delta\}$ , in one iteration by two different approaches, direct computation and the low-rank-matrix decomposition algorithm, for the numerical examples studied in this work with the same setups. We can see clearly that the improvement is dramatic.

#### Steps 4 and 5: computing gradient descent flows

Standard techniques apply; see Isakov et al. (2011) for details. Related techniques have been widely used in the level set community in various applications (Osher and Sethian, 1988; Qian and Symes, 2002a,b; Qian et al., 2003; Qian and Leung, 2004; Leung et al., 2004; Qian and Leung, 2006; Cecil et al., 2006; Leung et al., 2007). To avoid numerical instabilities as addressed in Isakov et al. (2011), the Heaviside function is approximated by the  $\epsilon$ -Heaviside function as:

$$H_\epsilon(\phi) = \begin{cases} 0, & \phi < -\epsilon, \\ \frac{1}{2} + \frac{\phi}{2\epsilon} + \frac{1}{2\pi} \sin\left(\frac{\pi\phi}{\epsilon}\right), & -\epsilon \leq \phi \leq \epsilon, \\ 1, & \phi > \epsilon. \end{cases} \quad (16)$$

## NUMERICAL RESULTS

We study several synthetic examples in terms of three different index sets:  $\mathbf{M} = \{xy, \Delta\}$ ,  $\mathbf{M} = \{zz\}$ , and  $\mathbf{M} = \{xy, \Delta, zz\}$ .

### Two cubes

We first study a two-cube model as shown in Figure 3(a), which was previously studied by Zhdanov et al. (2004). The target domain  $D$  consists of two identical cubes; they have sides of length 150m, are 150m under the surface and are 150m apart; the density contrast in both cubes over the background is  $1 \times 10^3 \text{kg/m}^3$ .

To be consistent with Zhdanov et al. (2004), we take the subsurface domain  $\Omega = [-275, 275] \text{m} \times [-325, 325] \text{m} \times [-500, 0] \text{m}$  and assume that there are  $21 \times 25 = 525$  observation points on the ground surface  $\Gamma = [-250, 250] \text{m} \times [-300, 300] \text{m} \times \{z = 0 \text{m}\}$ , which are uniformly distributed with grid size 25m in both  $x$ - and  $y$ - directions. To collect data  $g_{xy}$ ,  $g_\Delta$  and  $g_{zz}$ , we compute  $u_{xy}$ ,  $u_\Delta$  and  $u_{zz}$  by equation (6) and use the trapezoidal rule to approximate the volume integral over the domain  $D$ , which is assumed to be uniformly discretized with grid size 25m in all three directions. We further

add 3% Gaussian noise to the resulting  $u_{xy}$ ,  $u_{\Delta}$  and  $u_{zz}$ , and obtain the data-set  $\{g_{xy}, g_{\Delta}, g_{zz}\}$  as shown in Figures 3 (b-d).

To initialize the level-set algorithm, we employ both the migration method and the weighted  $L^1$ -regularization method to locate gravity centers of source bodies. In the implementation, we uniformly discretize  $\Omega$  into  $12 \times 14 \times 11$  mesh points with grid size 50m in all directions. We migrate four different data-sets:  $\{g_{xy}\}$ ,  $\{g_{\Delta}\}$ ,  $\{g_{zz}\}$  and  $\{g_{xy}, g_{\Delta}, g_{zz}\}$  to find corresponding migration densities; meanwhile, we compute the weighted  $L^1$ -regularized solution for the same four data-sets by solving Problem (15). From the eight numerical solutions, we capture extrema at  $x = 0$ m for both methods, as shown in Figures 4 and 5, where dashed lines show the true positions of source bodies.

Among the four migration densities shown in Figure 4, the migration density  $\rho_{\Delta}^*$  in Figure 4(b) resolves the two source bodies. In contrast, all four  $L^1$  regularization solutions in Figures 5 resolve the two source bodies. From extrema shown in Figure 4(b) and Figure 5, we initialize the level set function to be two well-separated spheres of the same radius 50m, centered at  $(0, -200, -150)$ m and  $(0, 50, -150)$ m, respectively.

To apply the level-set algorithm, we take  $\rho_0$  to be the exact value, i.e.,  $\rho_0 = 1 \times 10^3 \text{kg/m}^3$  and re-discretize the computational domain  $\Omega$  into  $23 \times 27 \times 21$  uniform mesh points with the same grid size 25m in all directions.

For all three index sets:  $\mathbf{M} = \{xy, \Delta\}$ ,  $\mathbf{M} = \{zz\}$  and  $\mathbf{M} = \{xy, \Delta, zz\}$ , we compute related numerical solutions based on the above setup. To compare the performance of the three index sets, in Figure 6 we plot shapes of the three numerical solutions at the 6000th iteration and cross sections of those solutions at  $x = 0$ m, where dashed lines show true positions of source bodies. We can see that for all three index sets, the level-set algorithm produces numerical solutions that match with true source bodies reasonably well and locate source bodies at true depths.

To test robustness of the level-set algorithm, we initialize the level set function to be a single sphere of radius 50m centered at  $(0, -200, -150)$ m and then compute numerical solutions for all

three index sets:  $\mathbf{M} = \{xy, \Delta\}$ ,  $\mathbf{M} = \{zz\}$  and  $\mathbf{M} = \{xy, \Delta, zz\}$ .

For  $\mathbf{M} = \{xy, \Delta\}$ , we plot numerical solutions at different iterations as shown in Figure 7. We can see that the level set algorithm succeeds in splitting the single source body into two and numerical solutions become steady after 4000 iterations. For the other two index sets:  $\mathbf{M} = \{zz\}$  and  $\mathbf{M} = \{xy, \Delta, zz\}$ , we compute numerical solutions by using the same initial level set function. In comparison with the true model, we show, for all three index sets, numerical solutions and their cross sections at  $x = 0\text{m}$  at the 6000th iteration in Figure 8. We can see that for all three index sets, the level-set algorithm even with an unreasonable initial guess still produces numerical solutions that match with true source bodies reasonably well and locate source bodies at true depths.

### Three cuboids

We next study a model with three source bodies, consisting of two short cuboids and one long cuboid, as shown in Figure 9(a). The density contrast in all source bodies is  $1 \times 10^3 \text{kg/m}^3$ . We take the computational domain  $\Omega = [0, 1]\text{km} \times [0, 1]\text{km} \times [-0.5, 0]\text{km}$  and assume that there are  $33 \times 33 = 1089$  observation points, uniformly distributed on the surface  $\Gamma = [0, 1]\text{km} \times [0, 1]\text{km} \times \{z = 0\text{km}\}$  with grid size  $1/32\text{km}$  in both  $x$ - and  $y$ - directions. To collect data  $g_{xy}$ ,  $g_{\Delta}$  and  $g_{zz}$ , we compute  $u_s$  by equation (6) for  $s = xy, \Delta, zz$  and use the trapezoidal rule to approximate the volume integral over the domain  $D$ , which is uniformly discretized with grid size  $1/32\text{km}$  in all three directions. We further add 3% Gaussian noise to the resulting  $u_{xy}$ ,  $u_{\Delta}$  and  $u_{zz}$ , and obtain the data-set  $\{g_{xy}, g_{\Delta}, g_{zz}\}$  as shown in Figures 9(b-d).

To initialize the level-set algorithm, we employ both the migration method and the weighted  $L^1$ -regularization method to locate gravity centers of source bodies. In the implementation, we uniformly discretize the computational domain  $\Omega$  into  $21 \times 21 \times 11$  mesh points with grid size  $0.05\text{km}$  in all directions. We migrate four different data-sets:  $\{g_{xy}\}$ ,  $\{g_{\Delta}\}$ ,  $\{g_{zz}\}$  and  $\{g_{xy}, g_{\Delta}, g_{zz}\}$  to find corresponding migration densities; meanwhile, we compute the weighted  $L^1$ -regularized solution for the same four data-sets by solving Problem (15). From the eight numerical solutions,

we capture only one extremum around the point  $(0.3, 0.3, -0.1)$ km, and therefore we initialize the level set function to be a single sphere of radius 0.09km centered at  $(0.3, 0.3, -0.1)$ km, as shown in Figure 10(a).

To apply the level-set algorithm, we take  $\rho_0$  to be the exact value, i.e.,  $\rho_0 = 1 \times 10^3 \text{kg/m}^3$  and re-discretize the computational domain  $\Omega$  into  $33 \times 33 \times 17$  uniform mesh points with the same grid size  $1/32$ km in all directions.

For  $\mathbf{M} = \{xy, \Delta\}$ , by the level-set algorithm we obtain numerical solutions at different iterations as shown in Figure 10. We can see that the level-set algorithm succeeds in resolving all source bodies completely after 4000 iterations, and numerical solutions converge to a steady state.

For the other two index sets,  $\mathbf{M} = \{zz\}$  and  $\mathbf{M} = \{xy, \Delta, zz\}$ , we compute related numerical solutions with the same setup. To compare the performance of the three index sets, in Figure 11 we plot shapes of the three numerical solutions at the 6000th iteration and cross sections of those solutions at  $y = 10/32$ km and  $y = 19/32$ km, where dashed lines show true positions of source bodies. We can see that for all three index sets, the level-set algorithm produces numerical solutions that match with true source bodies reasonably well and locate source bodies at true depths.

## Two dykes

We next study a more complicated model as shown in Figure 12 (a), where the target domain  $D$  consists of two well-separated dykes, and the density contrast of the short dyke is  $0.8 \text{g/cm}^3$  while that of the long dyke is  $1 \text{g/cm}^3$ . This example was previously studied in inversion of gravimetry data by Li and Oldenburg (1998), and we use this example to check applicability of the level-set algorithm to source bodies with different density contrasts.

To be consistent with Li and Oldenburg (1998), we take the subsurface domain  $\Omega = [0, 2] \text{km} \times [0, 2] \text{km} \times [-1, 0] \text{km}$  and assume that there are  $21 \times 41 = 861$  observation points on the surface  $\Gamma = [0, 2] \text{km} \times [0, 2] \text{km} \times \{z = 0 \text{km}\}$ , which are uniformly distributed with grid sizes 0.1km and 0.05km in

the  $x$ - direction and the  $y$ - direction, respectively. To collect the data-set  $\{g_{xy}, g_{\Delta}, g_{zz}\}$ , we compute  $u_{xy}$ ,  $u_{\Delta}$  and  $u_{zz}$  by equation (6) and use the trapezoidal rule to discretize the volume integral over the domain  $D$ , which is uniformly discretized with grid size 1/32km in all directions. We then add 5% Gaussian noise to the resulting  $u_{xy}$ ,  $u_{\Delta}$  and  $u_{zz}$ , and obtain the data-set  $\{g_{xy}, g_{\Delta}, g_{zz}\}$  as shown in Figures 12(b-d).

To initialize the level-set algorithm, we employ both the migration method and the weighted  $L^1$ -regularization method to locate gravity centers of source bodies. In the implementation, we uniformly discretize the computational domain  $\Omega$  into  $21 \times 21 \times 11$  mesh points with grid size 0.1km in all directions. We migrate four different data-sets:  $\{g_{xy}\}$ ,  $\{g_{\Delta}\}$ ,  $\{g_{zz}\}$  and  $\{g_{xy}, g_{\Delta}, g_{zz}\}$  to find corresponding migration densities; meanwhile, we compute the weighted  $L^1$ -regularized solution for the same four different data-sets by solving Problem (15). From the eight numerical solutions, we capture extrema at  $x = 1\text{km}$  for both methods, as shown in Figures 13 and 14, where dashed lines show the true positions of source bodies.

Among the four migration densities shown in Figure 13, the migration density  $\rho_{\Delta}^*$  in Figure 13(b) resolves the two source bodies. In contrast, all four  $L^1$  regularization solutions in Figure 14 resolve the two source bodies. From extrema shown in Figure 13(b) and Figure 14, we initialize the level set function to be two well-separated spheres of the same radius 0.1km, centered at  $(1.0, 0.7, -0.3)\text{km}$  and  $(1.0, 1.4, -0.3)\text{km}$ , respectively.

To apply the level-set algorithm, as the range of subsurface density contrasts is from  $0.8\text{g/cm}^3$  to  $1.0\text{g/cm}^3$ , we consider three different values of  $\rho_0$ : taking  $\rho_0 = 0.8\text{g/cm}^3$ ,  $\rho_0 = 0.9\text{g/cm}^3$  and  $\rho_0 = 1.0\text{g/cm}^3$ . We re-discretize the computational domain  $\Omega$  into  $65 \times 65 \times 33$  uniform mesh points with the same grid size 1/32km in all directions.

For the three index sets  $\mathbf{M} = \{xy, \Delta\}$ ,  $\mathbf{M} = \{zz\}$ , and  $\mathbf{M} = \{xy, \Delta, zz\}$ , by the level-set algorithm we obtain numerical solutions at the 2000th iteration, and their cross sections at  $x = 1\text{km}$  and at  $z = -0.25\text{km}$  as shown in Figures 15, 16 and 17, respectively. We can see that for all three different values of  $\rho_0$ , numerical solutions match with true models reasonably well and

locate source bodies at their true depths.

To test robustness of the level-set algorithm, we initialize the level set function to be a single sphere of radius 0.1km centered at (1.0, 0.7, -0.3)km and then compute numerical solutions for all three index sets:  $\mathbf{M} = \{xy, \Delta\}$ ,  $\mathbf{M} = \{zz\}$  and  $\mathbf{M} = \{xy, \Delta, zz\}$  with  $\rho_0 = 1.0\text{g/cm}^3$ . Numerical solutions at 2000th iteration and their cross sections at  $x = 1\text{km}$  and  $z = -0.25\text{km}$  are shown in Figure 18, where dashed lines indicate true positions of source bodies. We can see that although the level-set algorithm fails in resolving source bodies, cross sections shown in Figures 18(d-i) indicate that numerical solutions locate true positions of source bodies.

## CONCLUSION

We proposed a local level set method for the inversion of gravity gradient data. Assuming that a homogeneous density contrast distribution with the value of density contrast specified a priori is supported on an unknown bounded domain  $D$ , we were able to convert the original inverse problem into a domain inverse problem so that the level-set method can be applied to parametrize the unknown domain. We applied the migration method and a weighted  $L^1$ -regularization method to locate gravity centers of source bodies which may provide robust initialization for the level-set algorithm. We also developed a low-rank-matrix decomposition algorithm to compute rapidly the mismatch and the Frechet derivative. Extensive numerical experiments illustrate effectiveness of the local level set method.

## ACKNOWLEDGMENT

We thank the assistant editor Dr. Jeffrey Shragge, the associate editor Dr. Xiong Li, Dr. Gary Barnes, Dr. Colin Farquharson, and two anonymous reviewers for their many constructive and valuable comments and suggestions. Qian is supported by NSF-1222368.

## REFERENCES

- Barnes, G. J., and Barraud, J., 2012, Imaging geologic surfaces by inverting gravity gradient data with depth horizons: *Geophysics*, **77**, G1–G11.
- Barnes, G. J., Barraud, J., Lumley, J., and Davies, M., 2008, Advantages of multi-tensor, high resolution gravity gradient data: 78th Ann. Internat. Mtg., Soc. Expl. Geophys., Tulsa, OK, Expanded Abstracts, 3587–3590.
- Ben Hadj Miled, M. K., and Miller, E. L., 2007, A projection-based level-set approach to enhance conductivity anomaly reconstruction in electrical resistance tomography: *Inverse Problem*, **23**, 2375–2400.
- Brezis, H., 1974, Solutions with compact support of variational inequalities, dedicated to the memory of I. G. Petrovski: *Uspekhi Mat. Nauk*, **29**, 103–108.
- Burger, M., and Osher, S., 2005, A survey on level set methods for inverse problems and optimal design: *European J. Appl. Math.*, **16**, 263–301.
- Burger, M., 2001, A level set method for inverse problems: *Inverse Problems*, **17**, 1327–1356.
- Cecil, T., Osher, S. J., and Qian, J., 2006, Simplex free adaptive tree fast sweeping and evolution methods for solving level set equations in arbitrary dimension: *J. Comput. Phys.*, **213**, 458–473.
- Cella, F., and Fedi, M., 2012, Inversion of potential field data using the structural index as weighting function rate decay: *Geophysical Prospecting*, **60**, 313–336.
- Condi, F., and Talwani, M., 1999, Resolution and efficient inversion of gravity gradiometry: 70th Ann. Internat. Mtg., Soc. Expl. Geophys., Tulsa, OK, Expanded Abstracts, 358–361.
- Dorn, O., and Lesselier, D., 2006, Level set methods for inverse scattering: *Inverse Problems*, **22**, R67–R131.
- Farquharson, C. G., and Mosher, C. R. W., 2009, Three-dimensional modelling of gravity data using finite differences: *Journal of Applied Geophysics*, **68**, 417–422.

- Fedi, M., and Florio, G., 2006, SCALFUN: 3D analysis of potential field scaling function to determine independently or simultaneously structural index and depth to source: 77th Ann. Internat. Mtg., Soc. Expl. Geophys., Tulsa, OK, Expanded Abstracts, 963–967.
- Fedi, M., and Pilkington, M., 2012, Understanding imaging methods for potential field data: Geophysics, **77**, G13–G24.
- Fedi, M., 2007, DEXP: A fast method to determine the depth and the structural index of potential fields sources: Geophysics, **72**, I1–I11.
- Fullagar, P., and Pears, G., 2010, From gravity gradient to density gradient: The ASEG-PESA Airbone Gravity Workshop, Geoscience Australia, Abstracts from the ASEG-PESA Airbone Gravity Workshop, Geoscience Australia, Record 2010/23, 79–86.
- Hou, S., Solna, K., and Zhao, H.-K., 2004, Imaging of location and geometry for extended targets using the response matrix: J. Comput. Phys., **199**, 317–338.
- Isakov, V., Leung, S., and Qian, J., 2011, A fast local level set method for inverse gravimetry: Comm. in Computational Physics, **10**, 1044–1070.
- Isakov, V., Leung, S., and Qian, J., 2013, A three-dimensional inverse gravimetry problem for ice with snow caps: Inverse Problems and Imaging, **7**, 523–544.
- Jorgensen, G., and Kisabeth, J., 2000, Joint 3D inversion of gravity, magnetic and tensor gravity fields for imaging salt formations in the deepwater gulf of mexico: 71st Ann. Internat. Mtg., Soc. Expl. Geophys., Tulsa, OK, Expanded Abstracts, 424–426.
- Koh, K., Kim, S., and Boyd, S., 2007, l1\_ls: A Matlab Solver for Large-Scale l1–Regularized Least Squares Problems.: [[http://www.stanford.edu/~boyd/l1\\_ls/](http://www.stanford.edu/~boyd/l1_ls/)].
- Krahenbuhl, R., and Li, Y., 2006, Inversion of gravity data using a binary formulation: Geophysical Journal International, **167**, 543–556.
- Last, B. J., and Kubik, K., 1983, Compact gravity inversion: Geophysics, **48**, 713–721.

- Lee, J. B., 2010, FALCON gravity gradiometer technology: *Exploration Geophysics*, **32**, 247–250.
- Leung, S., Qian, J., and Osher, S. J., 2004, A level set method for three dimensional paraxial geometrical optics with multiple sources: *Comm. Math. Sci.*, **2**, 657–686.
- Leung, S., Qian, J., and Burridge, R., 2007, Eulerian Gaussian beams for high frequency wave propagation: *Geophysics*, **72**, SM61–SM76.
- Li, W., and Leung, S., 2013, A fast local level set based adjoint state method for first arrival transmission traveltimes tomography with discontinuous slowness: *Geophysical Journal International*, **195**, 582–596.
- Li, Y., and Oldenburg, D., 1998, 3D inversion of gravity data: *Geophysics*, **63**, 109–119.
- Li, Y., and Oldenburg, D., 2003, Fast inversion of large-scale magnetic data using wavelet transforms and a logarithmic barrier method: *Geophysical Journal International*, **152**, 251–265.
- Li, W., Leung, S., and Qian, J., 2014, A level set-adjoint state method for crosswell transmission-reflection traveltimes tomography: *Geophysical Journal International*, to appear, **xxx**, no. x, xxx.
- Li, Y., 2001a, 3D inversion of gravity gradiometer data: 72nd Ann. Internat. Mtg., Soc. Expl. Geophys., Tulsa, OK, Expanded Abstracts, 1470–1473.
- 2001b, Processing gravity gradiometer data using an equivalent source technique: 72nd Ann. Internat. Mtg., Soc. Expl. Geophys., Tulsa, OK, Expanded Abstracts, 1466–1469.
- Li, X., 2010, Efficient 3d gravity and magnetic modeling: *Electromagnetic, Gravity, and Magnetic (EGM) Methods International Workshop*, Extended Abstracts.
- Litman, A., Lesselier, D., and Santosa, F., 1998, Reconstruction of a 2-D binary obstacle by controlled evolution of a level-set: *Inverse Problems*, **14**, 685–706.
- Lu, W., Leung, S., and Qian, J., 2014, An improved fast local level set method for three-dimensional inverse gravimetry: submitted, **xx**, xxx–xxx.

- Martinez, C., Li, Y., Krahenbuhl, R., and Braga, M. A., 2010, 3D inversion of airborne gravity gradiometry for iron ore exploration in Brazil: 80th Ann. Internat. Mtg., Soc. Expl. Geophys., Tulsa, OK, Expanded Abstracts, 1753–1757.
- Martinez, C., Li, Y., Krahenbuhl, R., and Braga, M. A., 2013, 3D inversion of airborne gravity gradiometry data in mineral exploration; a case study in the Quadrilatero Ferrifero, Brazil: *Geophysics*, **78**, B1–B11.
- Osher, S. J., and Sethian, J. A., 1988, Fronts propagating with curvature dependent speed: algorithms based on Hamilton-Jacobi formulations: *J. Comput. Phys.*, **79**, 12–49.
- Ozolins, V., Lai, R., Caffisch, R., and Osher, S., 2013, Compressed modes for variational problems in mathematics and physics: *Proc. Natl. Acad. Sci. USA*, **110**, 18368–18373.
- Papadopoulos, D., Herty, M., Rath, V., and Behr, M., 2011, Identification of uncertainties in the shape of geophysical objects with level sets and the adjoint method: *Computational Geosciences*, **15**, 737–753.
- Pilkington, M., 2012, Analysis of gravity gradiometer inverse problems using optimal design measures: *Geophysics*, **77**, G25–G31.
- Portniaguine, O., and Zhdanov, M., 1999, Focusing geophysical inversion images: *Geophysics*, **64**, 874–887.
- Qian, J., and Leung, S., 2004, A level set method for paraxial multivalued traveltimes: *J. Comput. Phys.*, **197**, 711–736.
- Qian, J., and Leung, S., 2006, A local level set method for paraxial multivalued geometric optics: *SIAM J. Sci. Comp.*, **28**, 206–223.
- Qian, J., and Symes, W. W., 2002a, Adaptive finite difference method for traveltime and amplitude: *Geophysics*, **67**, 167–176.
- 2002b, Finite-difference quasi-P traveltimes for anisotropic media: *Geophysics*, **67**, 147–155.

- Qian, J., Cheng, L.-T., and Osher, S. J., 2003, A level set based Eulerian approach for anisotropic wave propagations: *Wave Motion*, **37**, 365–379.
- Routh, P., Jorgensen, G., and Kisabeth, J., 2001, Base of the salt imaging using gravity and tensor gravity data: 72nd Ann. Internat. Mtg., Soc. Expl. Geophys., Tulsa, OK, Expanded Abstracts, 1482–1484.
- Santosa, F., 1996, A level-set approach for inverse problems involving obstacles: *Control, Optimizat. Calculus Variat.*, **1**, 17–33.
- Sussman, M., Smereka, P., and Osher, S. J., 1994, A level set approach for computing solutions to incompressible two-phase flows: *J. Comput. Phys.*, **114**, 146–159.
- van den Doel, K., Ascher, U., and Leitao, A., 2010, Multiple level sets for piecewise constant surface reconstruction in highly ill-posed problems: *J. Sci. Comput.*, **43**, 44–66.
- Zhao, H.-K., Chan, T., Merriman, B., and Osher, S. J., 1996, A variational level set approach for multiphase motion: *J. Comput. Phys.*, **127**, 179–195.
- Zhdanov, M., Ellis, R., and Mukherjee, S., 2004, Three dimensional regularized focusing inversion of gravity gradient tensor component data: *Geophysics*, **69**, 925–937.
- Zhdanov, M., Liu, X., Wilson, G., and Wan, L., 2011, Potential field migration for rapid imaging of gravity gradiometry data: *Geophysical Prospecting*, **59**, 1052–1071.
- Zheglova, P., Farquharson, C. G., and Hurich, C. A., 2013, 2-D reconstruction of boundaries with level set inversion of traveltiems: *Geophysical Journal International*, **192**, 688–698.

## LIST OF FIGURES

1 Point-source model. (a): source point  $\mathbf{r}_s = [0.5, 1.5, -0.15]$ km marked by ‘\*’ underneath the measurement surface  $\Gamma = [0, 1]$ km  $\times$   $[1, 2]$ km  $\times$   $\{z = 0.1$ km $\}$ . Patterns of data, (b):  $g_{xy}$ , (c):  $g_{\Delta}$ , and (d):  $g_{zz}$  on  $\Gamma$  (unit:  $1\text{E} = 10^{-9}\text{s}^{-2}$ ).

2 Point-source model. Shapes of exact solutions: (a, d, g) with  $R = 0.13$ km in (a),  $R = 0.1$ km in (d) and  $R = 0.08$ km in (g). Shapes of numerical solutions: (b, e, h) for data  $g_{xy}$  and  $g_{\Delta}$ , and (c, f, i) for data  $g_{zz}$ .  $\rho_0 = 1\text{E}/\gamma/(4/3\pi(R/\text{km})^3)$  with  $R = 0.13$ km in (b, c),  $R = 0.1$ km in (e, f), and  $R = 0.08$ km in (h, i).

3 Two cubes. (a): true positions of the source bodies. Observed data (b):  $g_{xy}$ , (c):  $g_{\Delta}$ , and (d):  $g_{zz}$  on the ground surface  $\Gamma = [-250, 250]$ m  $\times$   $[-300, 300]$ m  $\times$   $\{z = 0$ m $\}$  polluted with 3% Gaussian noise (unit: E).

4 Two cubes. Cross sections of migration density at  $x = 0$ m by migrating single-index data (a):  $g_{xy}$ , (b):  $g_{\Delta}$ , (c):  $g_{zz}$ , and combined data (d):  $g_{xy}$ ,  $g_{\Delta}$  and  $g_{zz}$ .

5 Two cubes. Cross sections of  $L^1$  regularization solutions at  $x = 0$ m for single-index data (a):  $g_{xy}$ , (b):  $g_{\Delta}$ , (c):  $g_{zz}$ , and combined data (d):  $g_{xy}$ ,  $g_{\Delta}$  and  $g_{zz}$ . Dashed lines indicate the true positions of source bodies.

6 Two cubes with  $\rho_0 = 1 \times 10^3\text{kg}/\text{m}^3$ . Shapes of numerical solutions at the 6000th iteration with a two-sphere initial guess for the index set (a)  $\mathbf{M} = \{xy, \Delta\}$ , (c)  $\mathbf{M} = \{zz\}$ , and (e)  $\mathbf{M} = \{xy, \Delta, zz\}$ . Cross sections of solutions in (a, c, e) at  $x = 0$ m are plotted with solid lines in (b, d, f), respectively. Dashed rectangles indicate the true positions of source bodies.

7 Two cubes with  $\rho_0 = 1 \times 10^3\text{kg}/\text{m}^3$  and the index set  $\mathbf{M} = \{xy, \Delta\}$ . Shapes of the level set function at the (a) 0th (the initial guess being a sphere of radius 50m centered at  $(0, -200, -150)$ m), (b) 2000th, (c) 4000th, and (d) 6000th iteration.

8 Two cubes with  $\rho_0 = 1 \times 10^3\text{kg}/\text{m}^3$ . Shapes of numerical solutions with an one-sphere initial guess at the 6000th iteration for (a)  $\mathbf{M} = \{xy, \Delta\}$ , (c)  $\mathbf{M} = \{zz\}$ , and (e)  $\mathbf{M} = \{xy, \Delta, zz\}$ . Cross sections of solutions in (a, c, e) at  $x = 0$ m are plotted with solid lines in (b, d, f), respectively. Dashed rectangles indicate the true positions of source bodies.

9 Three cuboids. (a): true positions of the source bodies with  $\rho_0 = 1 \times 10^3 \text{kg/m}^3$ . Observed data polluted with 3% Gaussian noise (unit: E) in (b):  $g_{xy}$ , (c):  $g_{\Delta}$ , and (d)  $g_{zz}$  on the ground surface  $\Gamma = [0, 1] \text{km} \times [0, 1] \text{km} \times \{z = 0 \text{km}\}$ .

10 Three cuboids with  $\rho_0 = 1 \times 10^3 \text{kg/m}^3$  and  $\mathbf{M} = \{xy, \Delta\}$ . Shapes of the level set function at the (a) 0th (the initial guess being a sphere of radius 0.09km centered at (0.3, 0.3, -0.1)km), (b) 2000th, (c) 4000th, and (d) 6000th iteration.

11 Three cuboids with  $\rho_0 = 1 \times 10^3 \text{kg/m}^3$ . Shapes of numerical solutions at the 6000th iteration for (a)  $\mathbf{M} = \{xy, \Delta, zz\}$ , (d)  $\mathbf{M} = \{zz\}$ , and (g)  $\mathbf{M} = \{xy, \Delta, zz\}$ . Cross sections of solutions in (a, d, g) at  $y = 10/32 \text{km}$  plotted with solid lines in (b, e, h), respectively. Cross sections of solutions in (a, d, g) at  $y = 19/32 \text{km}$  plotted with solid lines in (c, f, i), respectively. Dashed rectangles indicate the true positions of source bodies.

12 Two dykes. (a): true positions of the source bodies, where  $\rho_0 = 0.8 \text{g/cm}^3$  in the short dyke while  $\rho_0 = 1.0 \text{g/cm}^3$  in the long dyke. Observed data (b)  $g_{xy}$ , (c)  $g_{\Delta}$ , and (d)  $g_{zz}$  on the ground surface  $\Gamma = [0, 2] \text{km} \times [0, 2] \text{km} \times \{z = 0 \text{km}\}$ ; all are polluted by 5% Gaussian noise.

13 Two dykes. Cross sections of the migration density at  $x = 1 \text{km}$  by migrating single-index data  $g_{xy}$  in (a),  $g_{\Delta}$  in (b), and  $g_{zz}$  in (c), and combined data  $g_{xy}$ ,  $g_{\Delta}$  and  $g_{zz}$  in (d).

14 Two dykes. Cross sections of  $L^1$  regularized solutions at  $x = 1 \text{km}$  for single-index data  $g_{xy}$  in (a),  $g_{\Delta}$  in (b),  $g_{zz}$  in (c), and combined data  $g_{xy}$ ,  $g_{\Delta}$  and  $g_{zz}$  in (d). Dashed lines indicate the true positions of source bodies.

15 Two dykes. Shapes of numerical solutions at the 2000th iteration with the index set  $\mathbf{M} = \{xy, \Delta\}$  and a two-sphere initial guess. (a):  $\rho_0 = 0.8 \text{g/cm}^3$ , (b):  $\rho_0 = 0.9 \text{g/cm}^3$ , and (c):  $\rho_0 = 1.0 \text{g/cm}^3$ . (d-f): cross sections of the numerical solutions in (a-c) at  $x = 1 \text{km}$ . (g-i): cross sections of the numerical solutions in (a-c) at  $z = -0.25 \text{km}$ . Dashed lines indicate the true positions of the target.

16 Two dykes. Shapes of numerical solutions at the 2000th iteration with the index set  $\mathbf{M} = \{zz\}$  and a two-sphere initial guess. (a):  $\rho_0 = 0.8 \text{g/cm}^3$ , (b):  $\rho_0 = 0.9 \text{g/cm}^3$ , and (c):  $\rho_0 = 1.0 \text{g/cm}^3$ . (d-f): cross sections of the numerical solutions in (a-c) at  $x = 1 \text{km}$ . (g-i): cross

sections of the numerical solutions in (a-c) at  $z = -0.25\text{km}$ . Dashed lines indicate the true positions of the target.

17 Two dykes. Shapes of numerical solutions at the 2000th iteration with the index set  $\mathbf{M} = \{xy, \Delta, zz\}$  and a two-sphere initial guess. (a):  $\rho_0 = 0.8\text{g/cm}^3$ ; (b):  $\rho_0 = 0.9\text{g/cm}^3$  and (c):  $\rho_0 = 1.0\text{g/cm}^3$ . (d-f): cross sections of the numerical solutions in (a-c) at  $x = 1\text{km}$ . (g-i): cross sections of the numerical solutions in (a-c) at  $z = -0.25\text{km}$ . Dashed lines indicate the true positions of the target.

18 Two dykes. Shapes of numerical solutions at the 2000th iteration for  $\rho = 1.0\text{g/cm}^3$  with a one-sphere initial guess for different index sets. (a):  $\mathbf{M} = \{xy, \Delta\}$ ; (b):  $\mathbf{M} = \{zz\}$ ; and (c):  $\mathbf{M} = \{xy, \Delta, zz\}$ . (d-f): cross sections of the numerical solutions in (a-c) at  $x = 1\text{km}$ . (g-i): cross sections of the numerical solutions in (a-c) at  $z = -0.25\text{km}$ . Dashed lines indicate the true positions of the target.

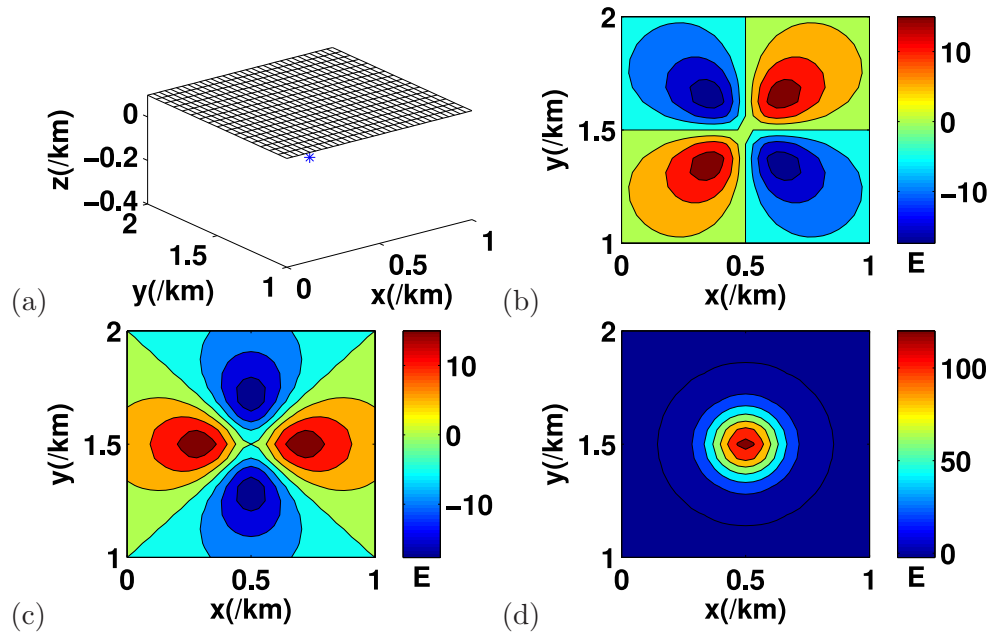


Figure 1: Point-source model. (a): source point  $\mathbf{r}_s = [0.5, 1.5, -0.15]$ km marked by ‘\*’ underneath the measurement surface  $\Gamma = [0, 1]\text{km} \times [1, 2]\text{km} \times \{z = 0.1\text{km}\}$ . Patterns of data, (b):  $g_{xy}$ , (c):  $g_{\Delta}$ , and (d):  $g_{zz}$  on  $\Gamma$  (unit:  $1\text{E} = 10^{-9}\text{s}^{-2}$ ).

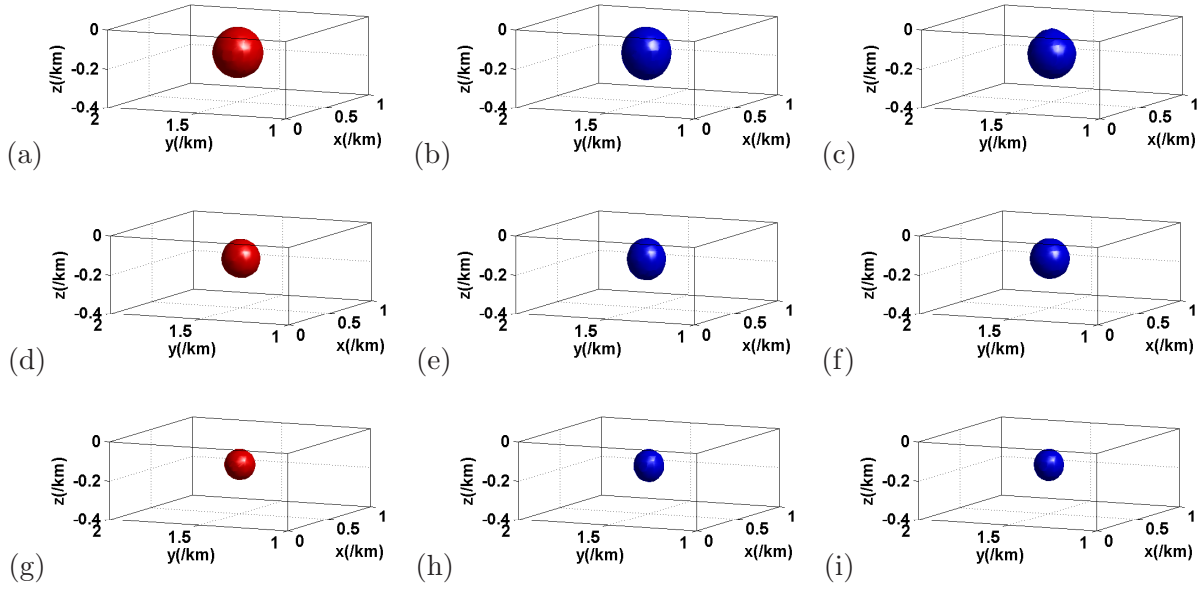


Figure 2: Point-source model. Shapes of exact solutions: (a, d, g) with  $R = 0.13\text{km}$  in (a),  $R = 0.1\text{km}$  in (d) and  $R = 0.08\text{km}$  in (g). Shapes of numerical solutions: (b, e, h) for data  $g_{xy}$  and  $g_{\Delta}$ , and (c, f, i) for data  $g_{zz}$ .  $\rho_0 = 1\text{E}/\gamma/(4/3\pi(R/\text{km})^3)$  with  $R = 0.13\text{km}$  in (b, c),  $R = 0.1\text{km}$  in (e, f), and  $R = 0.08\text{km}$  in (h, i).

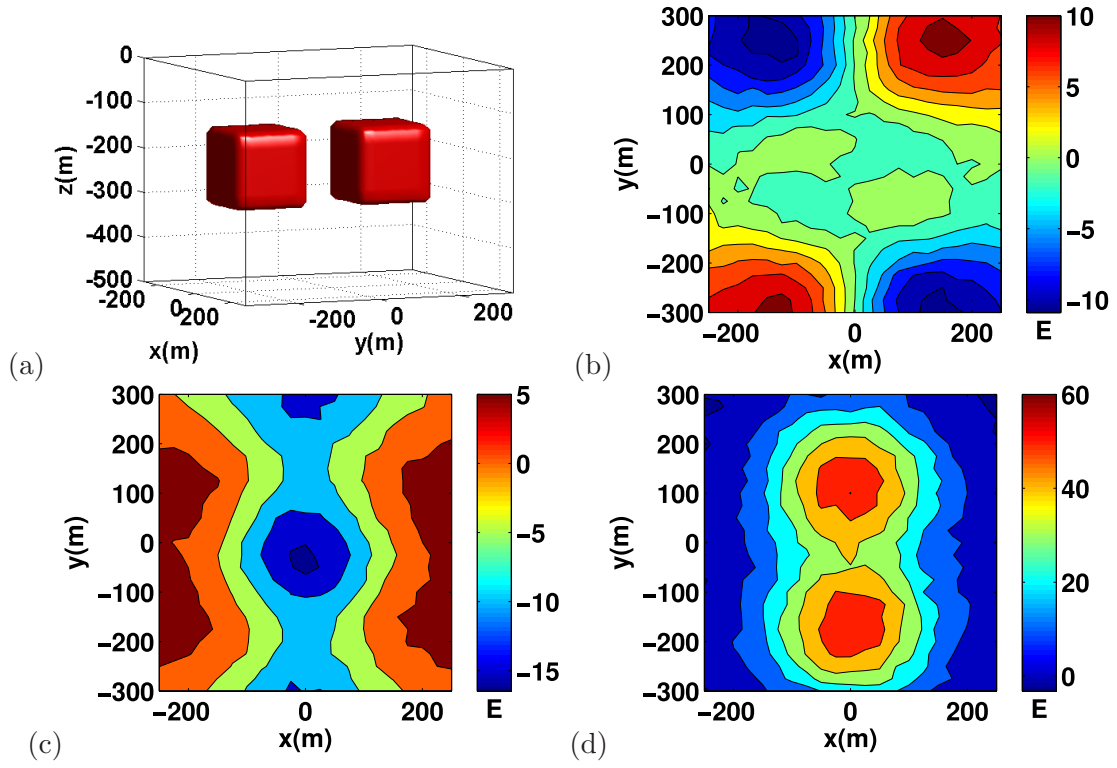


Figure 3: Two cubes. (a): true positions of the source bodies. Observed data (b):  $g_{xy}$ , (c):  $g_{\Delta}$ , and (d):  $g_{zz}$  on the ground surface  $\Gamma = [-250, 250]\text{m} \times [-300, 300]\text{m} \times \{z = 0\text{m}\}$  polluted with 3% Gaussian noise (unit: E).

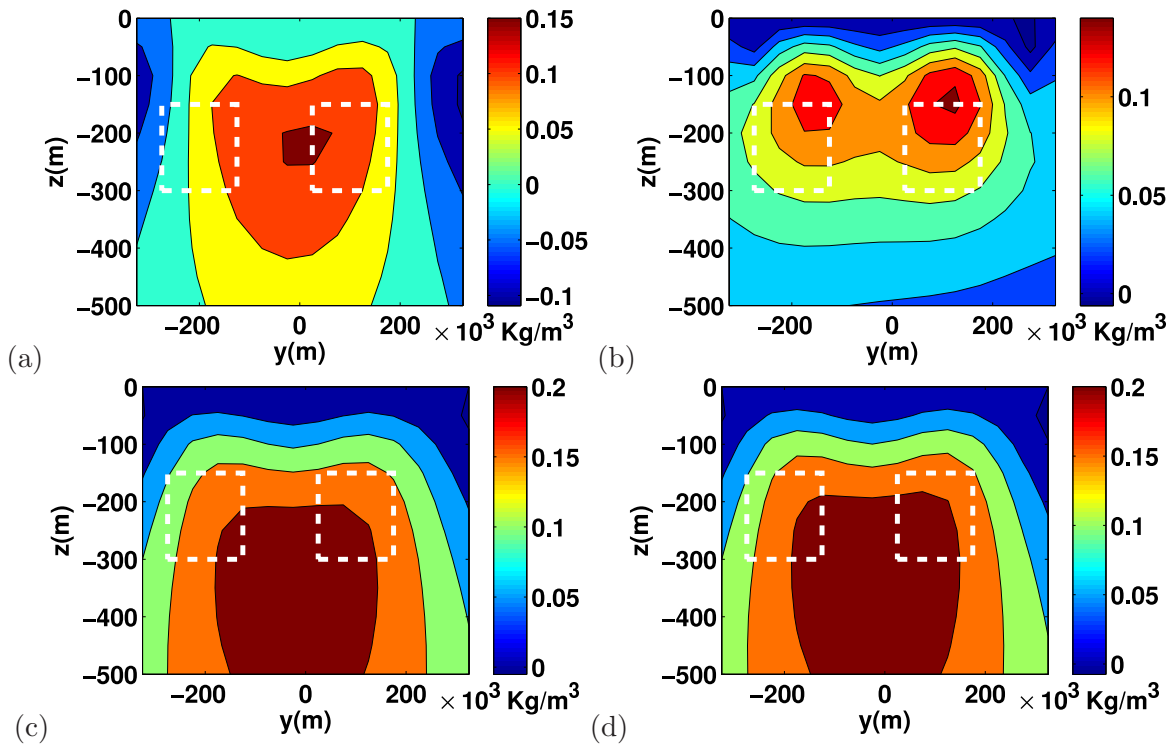


Figure 4: Two cubes. Cross sections of migration density at  $x = 0\text{m}$  by migrating single-index data (a):  $g_{xy}$ , (b):  $g_{\Delta}$ , (c):  $g_{zz}$ , and combined data (d):  $g_{xy}$ ,  $g_{\Delta}$  and  $g_{zz}$ .

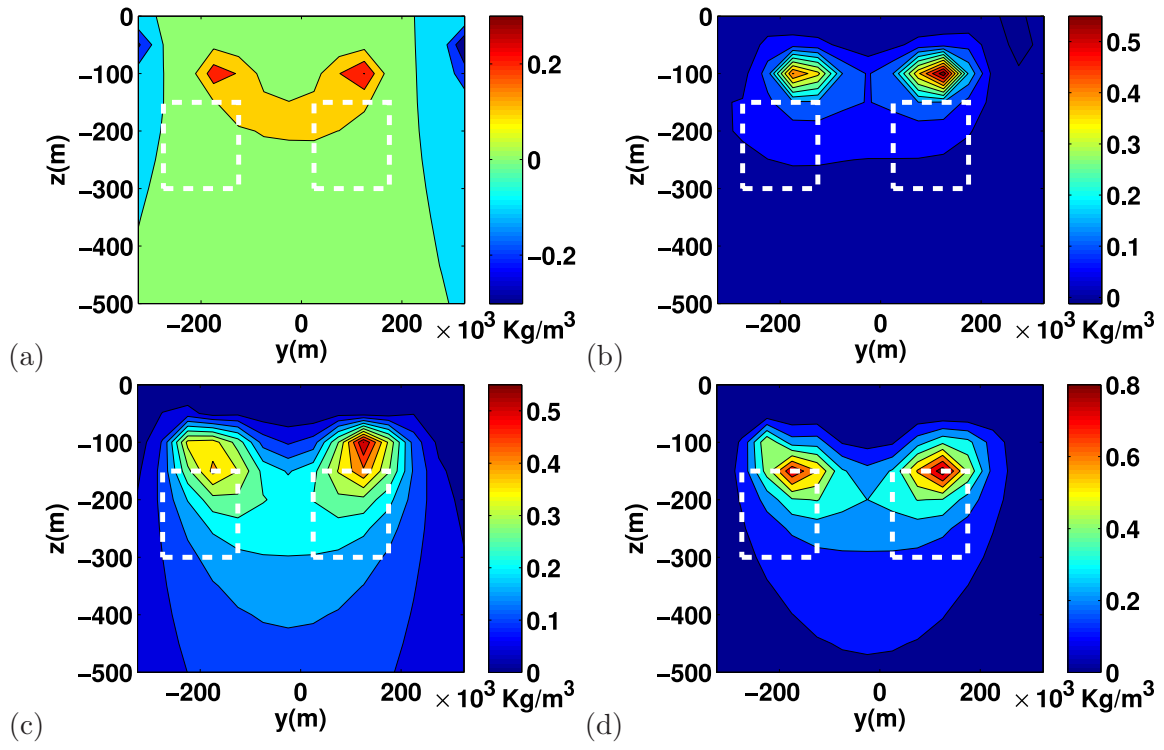


Figure 5: Two cubes. Cross sections of  $L^1$  regularization solutions at  $x = 0\text{m}$  for single-index data (a):  $g_{xy}$ , (b):  $g_{\Delta}$ , (c):  $g_{zz}$ , and combined data (d):  $g_{xy}$ ,  $g_{\Delta}$  and  $g_{zz}$ . Dashed lines indicate the true positions of source bodies.

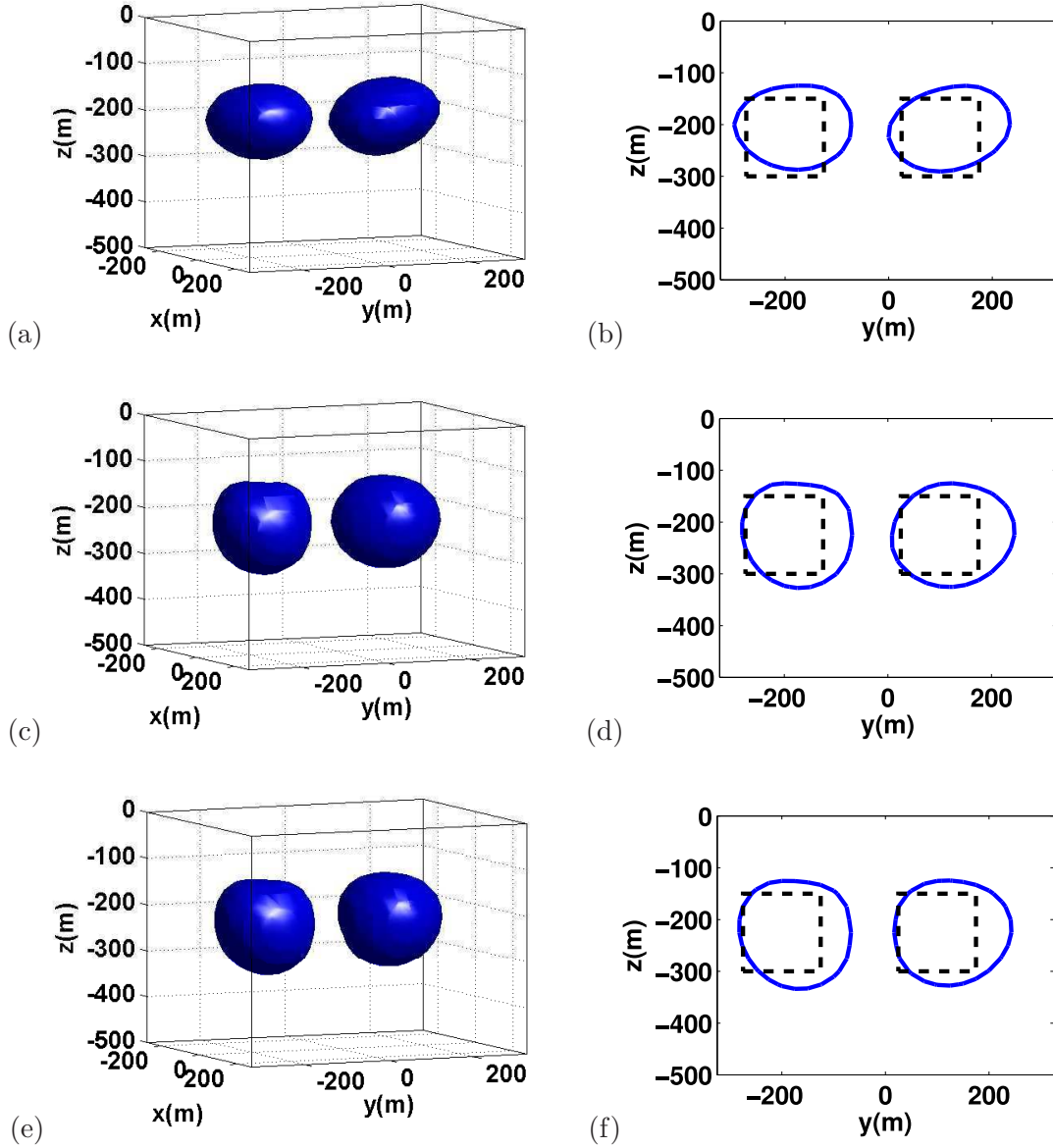


Figure 6: Two cubes with  $\rho_0 = 1 \times 10^3 \text{kg/m}^3$ . Shapes of numerical solutions at the 6000th iteration with a two-sphere initial guess for the index set (a)  $M = \{xy, \Delta\}$ , (c)  $M = \{zz\}$ , and (e)  $M = \{xy, \Delta, zz\}$ . Cross sections of solutions in (a, c, e) at  $x = 0$  m are plotted with solid lines in (b, d, f), respectively. Dashed rectangles indicate the true positions of source bodies.

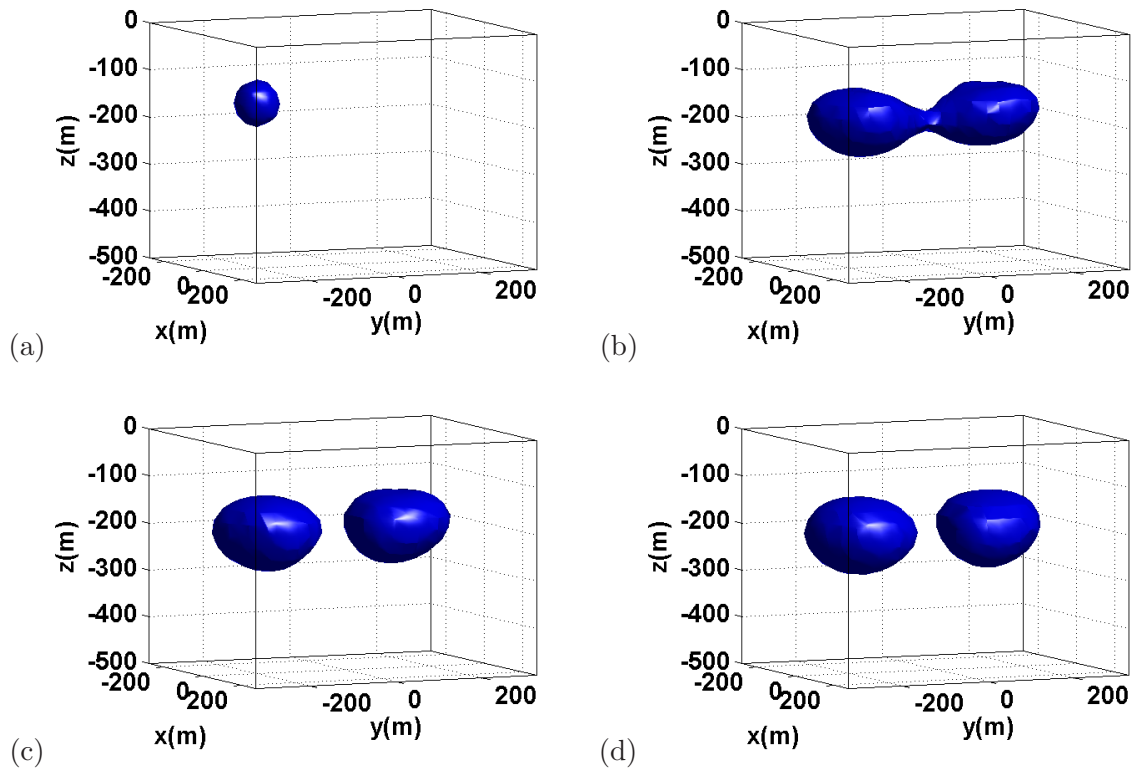


Figure 7: Two cubes with  $\rho_0 = 1 \times 10^3 \text{kg/m}^3$  and the index set  $M = \{xy, \Delta\}$ . Shapes of the level set function at the (a) 0th (the initial guess being a sphere of radius 50m centered at  $(0, -200, -150)\text{m}$ ), (b) 2000th, (c) 4000th, and (d) 6000th iteration.

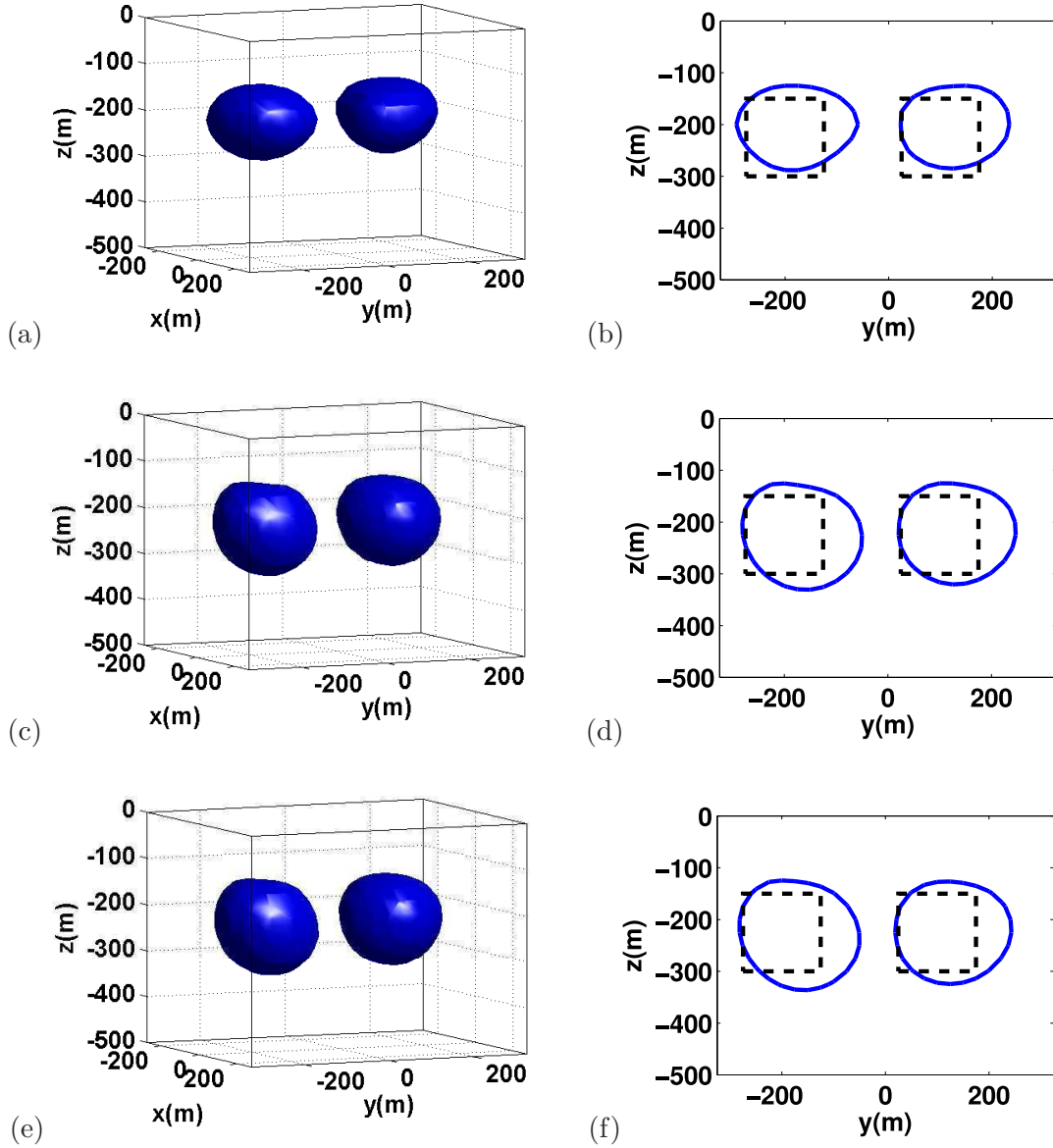


Figure 8: Two cubes with  $\rho_0 = 1 \times 10^3 \text{kg/m}^3$ . Shapes of numerical solutions with an one-sphere initial guess at the 6000th iteration for (a)  $M = \{xy, \Delta\}$ , (c)  $M = \{zz\}$ , and (e)  $M = \{xy, \Delta, zz\}$ . Cross sections of solutions in (a, c, e) at  $x = 0\text{m}$  are plotted with solid lines in (b, d, f), respectively. Dashed rectangles indicate the true positions of source bodies.

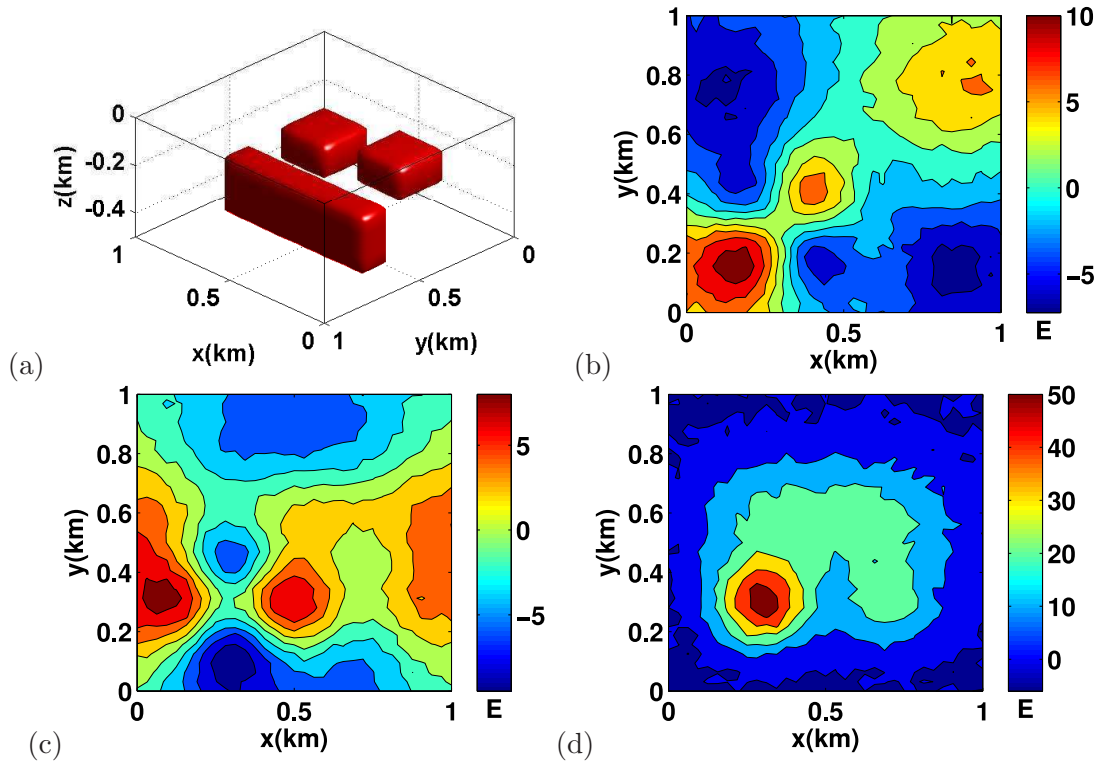


Figure 9: Three cuboids. (a): true positions of the source bodies with  $\rho_0 = 1 \times 10^3 \text{ kg/m}^3$ . Observed data polluted with 3% Gaussian noise (unit: E) in (b):  $g_{xy}$ , (c):  $g_{\Delta}$ , and (d)  $g_{zz}$  on the ground surface  $\Gamma = [0, 1] \text{ km} \times [0, 1] \text{ km} \times \{z = 0 \text{ km}\}$ .

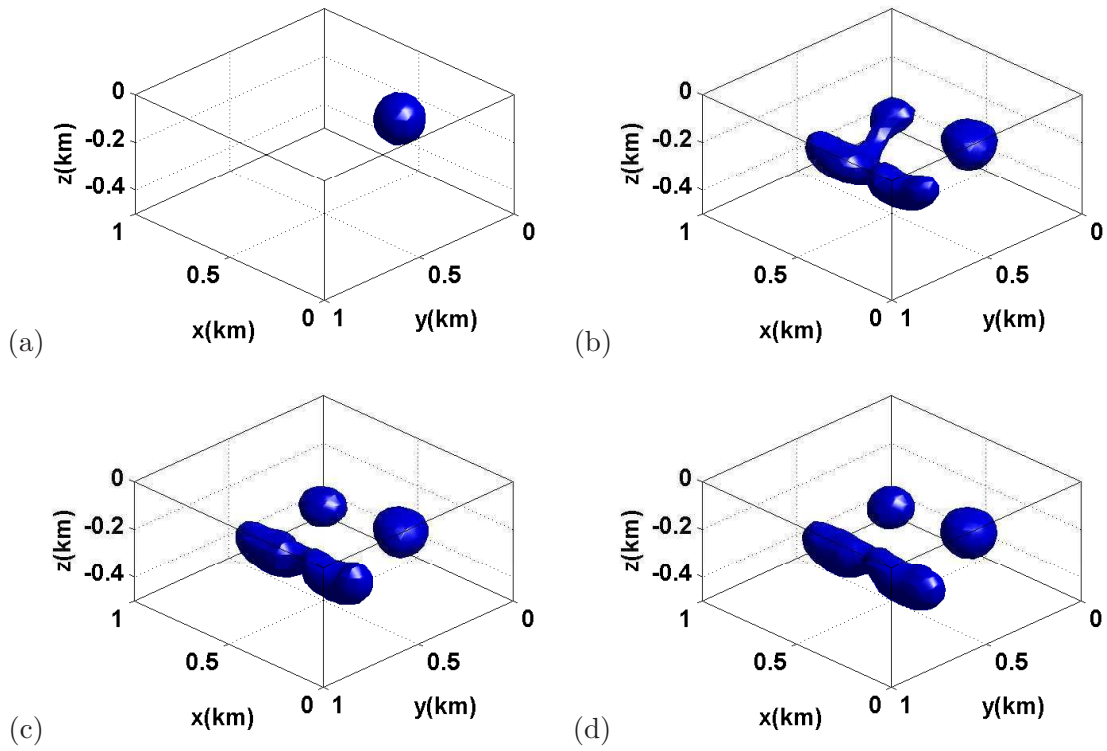


Figure 10: Three cuboids with  $\rho_0 = 1 \times 10^3 \text{kg/m}^3$  and  $M = \{xy, \Delta\}$ . Shapes of the level set function at the (a) 0th (the initial guess being a sphere of radius 0.09km centered at  $(0.3, 0.3, -0.1)$ km), (b) 2000th, (c) 4000th, and (d) 6000th iteration.

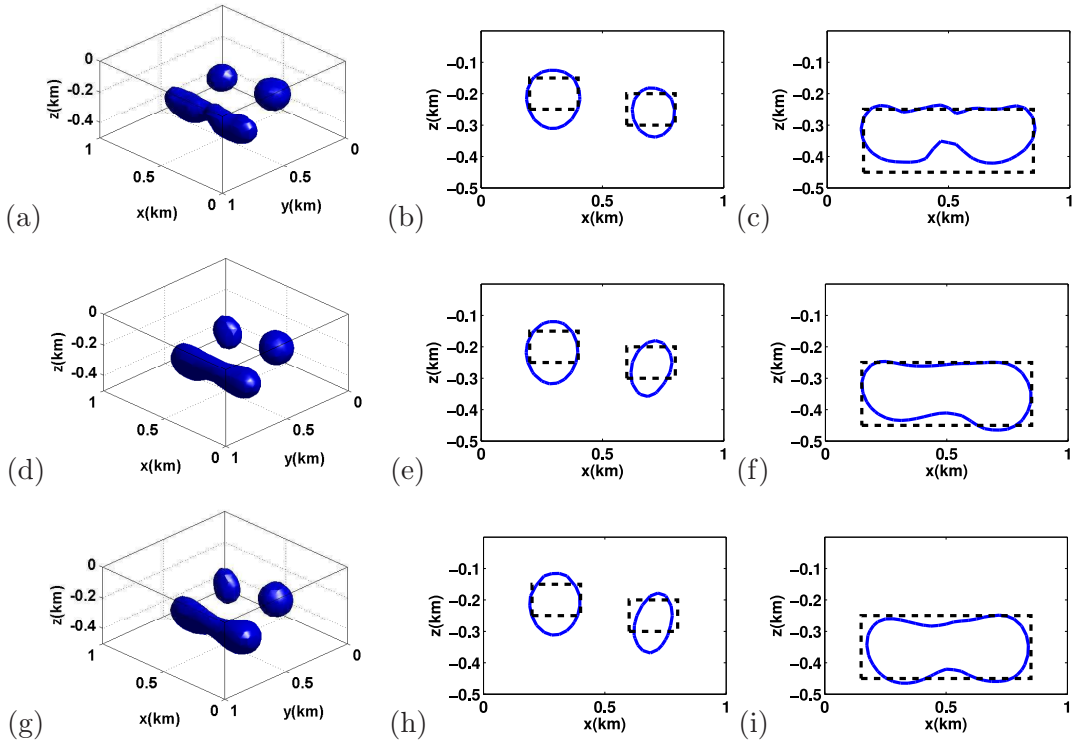


Figure 11: Three cuboids with  $\rho_0 = 1 \times 10^3 \text{kg/m}^3$ . Shapes of numerical solutions at the 6000th iteration for (a)  $\mathbf{M} = \{xy, \Delta, zz\}$ , (d)  $\mathbf{M} = \{zz\}$ , and (g)  $\mathbf{M} = \{xy, \Delta, zz\}$ . Cross sections of solutions in (a, d, g) at  $y = 10/32$  km plotted with solid lines in (b, e, h), respectively. Cross sections of solutions in (a, d, g) at  $y = 19/32$  km plotted with solid lines in (c, f, i), respectively. Dashed rectangles indicate the true positions of source bodies.

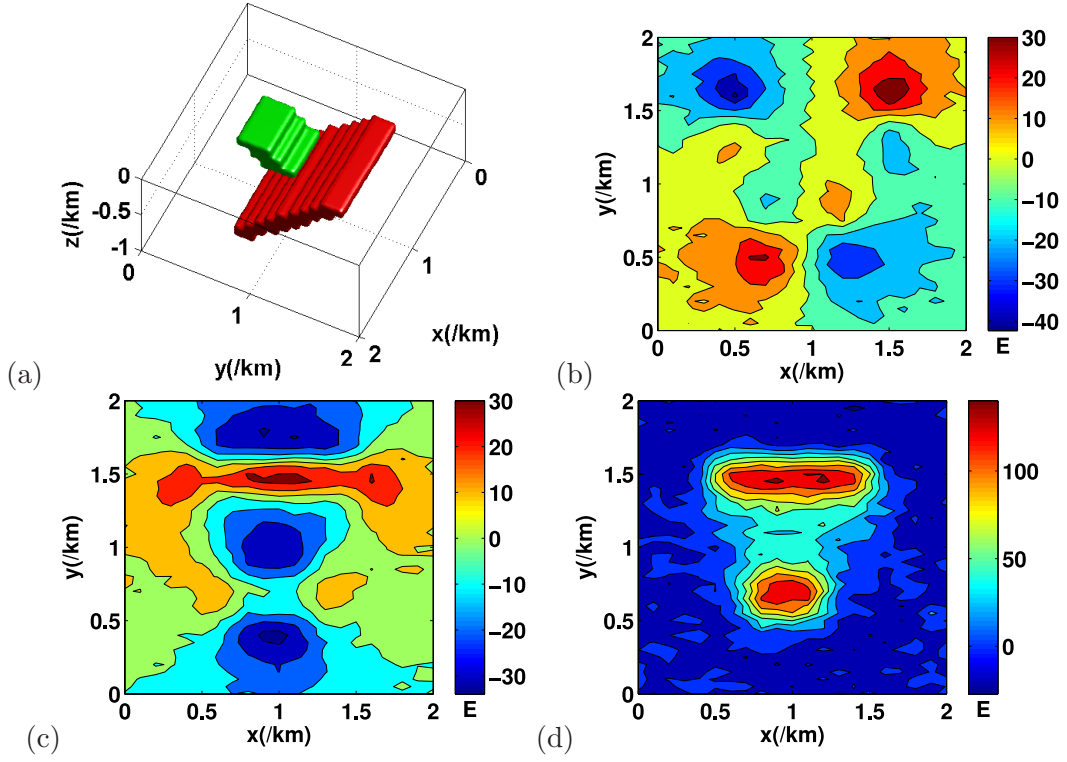


Figure 12: Two dykes. (a): true positions of the source bodies, where  $\rho_0 = 0.8\text{g/cm}^3$  in the short dyke while  $\rho_0 = 1.0\text{g/cm}^3$  in the long dyke. Observed data (b)  $g_{xy}$ , (c)  $g_{\Delta}$ , and (d)  $g_{zz}$  on the ground surface  $\Gamma = [0, 2]\text{km} \times [0, 2]\text{km} \times \{z = 0\text{km}\}$ ; all are polluted by 5% Gaussian noise.

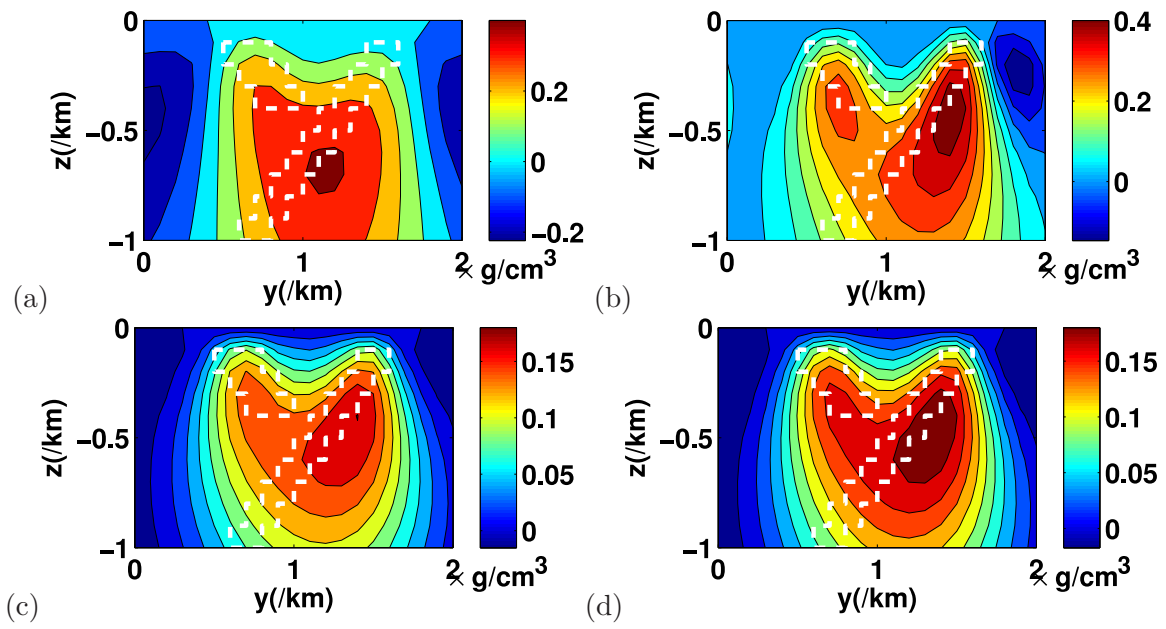


Figure 13: Two dykes. Cross sections of the migration density at  $x = 1\text{km}$  by migrating single-index data  $g_{xy}$  in (a),  $g_{\Delta}$  in (b), and  $g_{zz}$  in (c), and combined data  $g_{xy}$ ,  $g_{\Delta}$  and  $g_{zz}$  in (d).

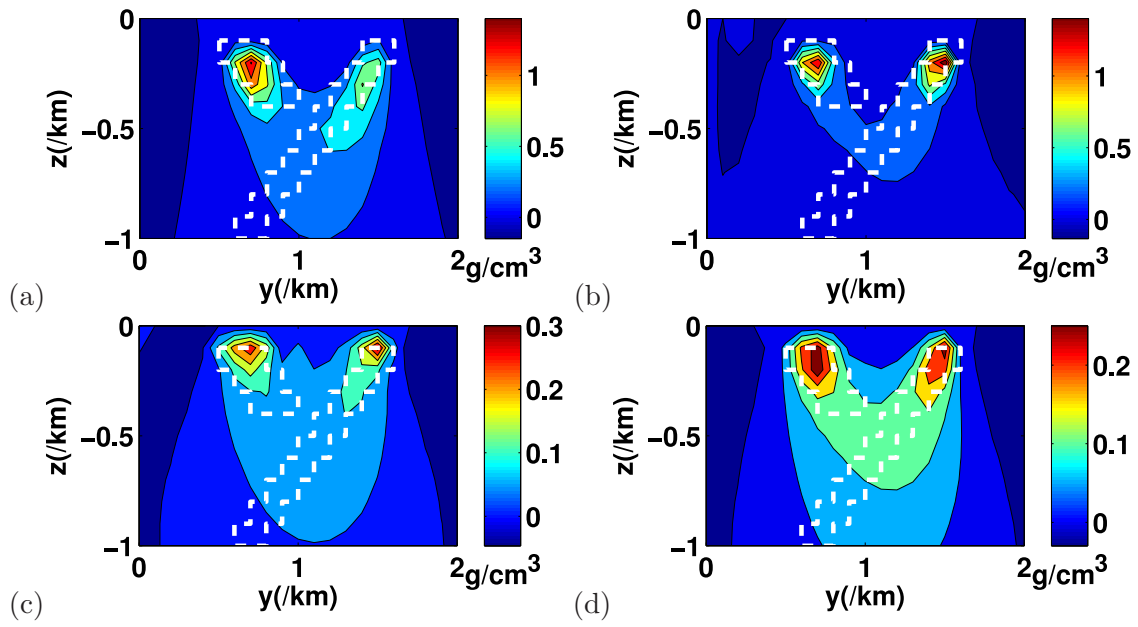


Figure 14: Two dykes. Cross sections of  $L^1$  regularized solutions at  $x = 1\text{km}$  for single-index data  $g_{xy}$  in (a),  $g_{\Delta}$  in (b),  $g_{zz}$  in (c), and combined data  $g_{xy}$ ,  $g_{\Delta}$  and  $g_{zz}$  in (d). Dashed lines indicate the true positions of source bodies.

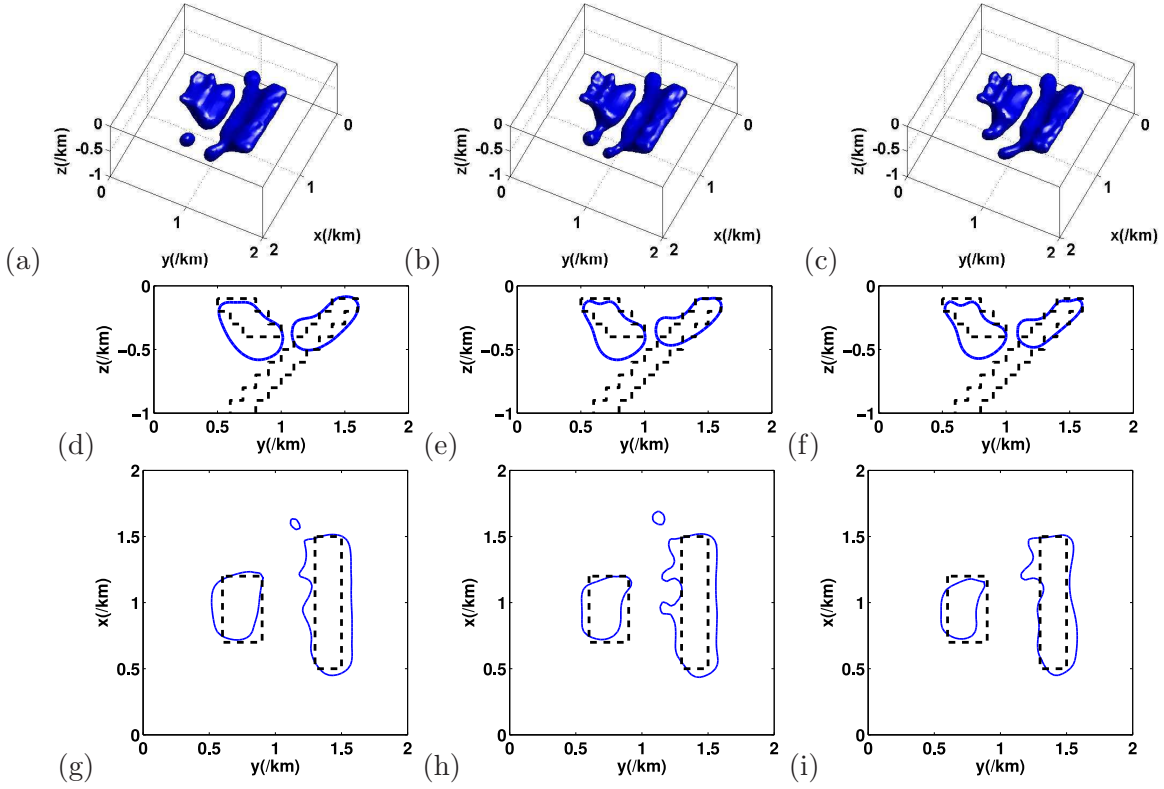


Figure 15: Two dykes. Shapes of numerical solutions at the 2000th iteration with the index set  $\mathbf{M} = \{xy, \Delta\}$  and a two-sphere initial guess. (a):  $\rho_0 = 0.8\text{g/cm}^3$ , (b):  $\rho_0 = 0.9\text{g/cm}^3$ , and (c):  $\rho_0 = 1.0\text{g/cm}^3$ . (d-f): cross sections of the numerical solutions in (a-c) at  $x = 1\text{km}$ . (g-i): cross sections of the numerical solutions in (a-c) at  $z = -0.25\text{km}$ . Dashed lines indicate the true positions of the target.

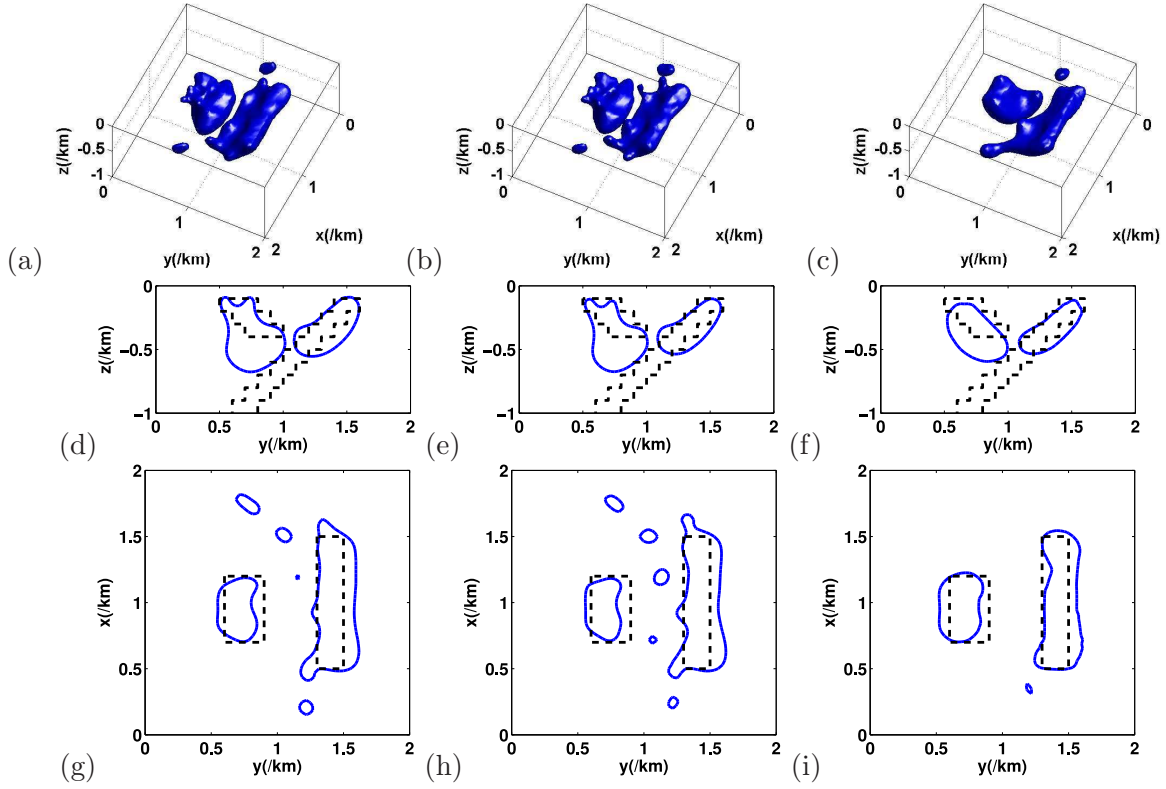


Figure 16: Two dykes. Shapes of numerical solutions at the 2000th iteration with the index set  $\mathbf{M} = \{zz\}$  and a two-sphere initial guess. (a):  $\rho_0 = 0.8\text{g/cm}^3$ , (b):  $\rho_0 = 0.9\text{g/cm}^3$ , and (c):  $\rho_0 = 1.0\text{g/cm}^3$ . (d-f): cross sections of the numerical solutions in (a-c) at  $x = 1\text{km}$ . (g-i): cross sections of the numerical solutions in (a-c) at  $z = -0.25\text{km}$ . Dashed lines indicate the true positions of the target.

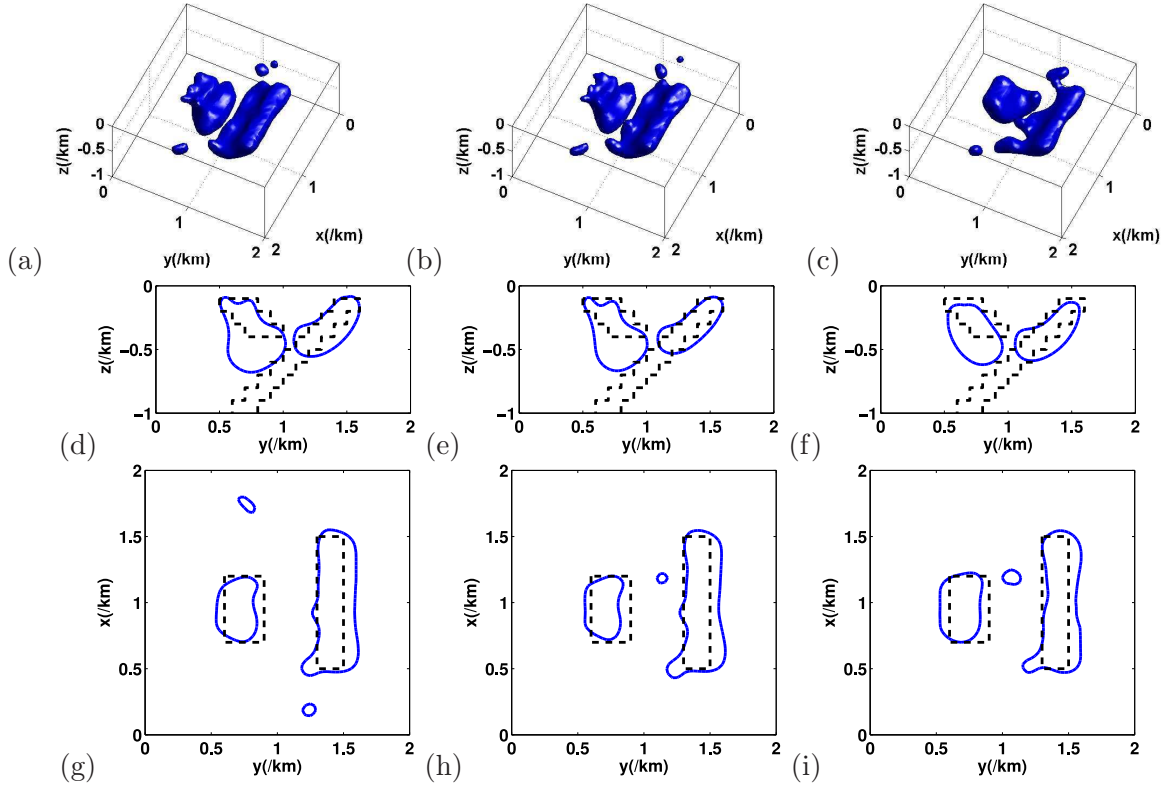


Figure 17: Two dykes. Shapes of numerical solutions at the 2000th iteration with the index set  $\mathbf{M} = \{xy, \Delta, zz\}$  and a two-sphere initial guess. (a):  $\rho_0 = 0.8\text{g/cm}^3$ ; (b):  $\rho_0 = 0.9\text{g/cm}^3$  and (c):  $\rho_0 = 1.0\text{g/cm}^3$ . (d-f): cross sections of the numerical solutions in (a-c) at  $x = 1\text{km}$ . (g-i): cross sections of the numerical solutions in (a-c) at  $z = -0.25\text{km}$ . Dashed lines indicate the true positions of the target.

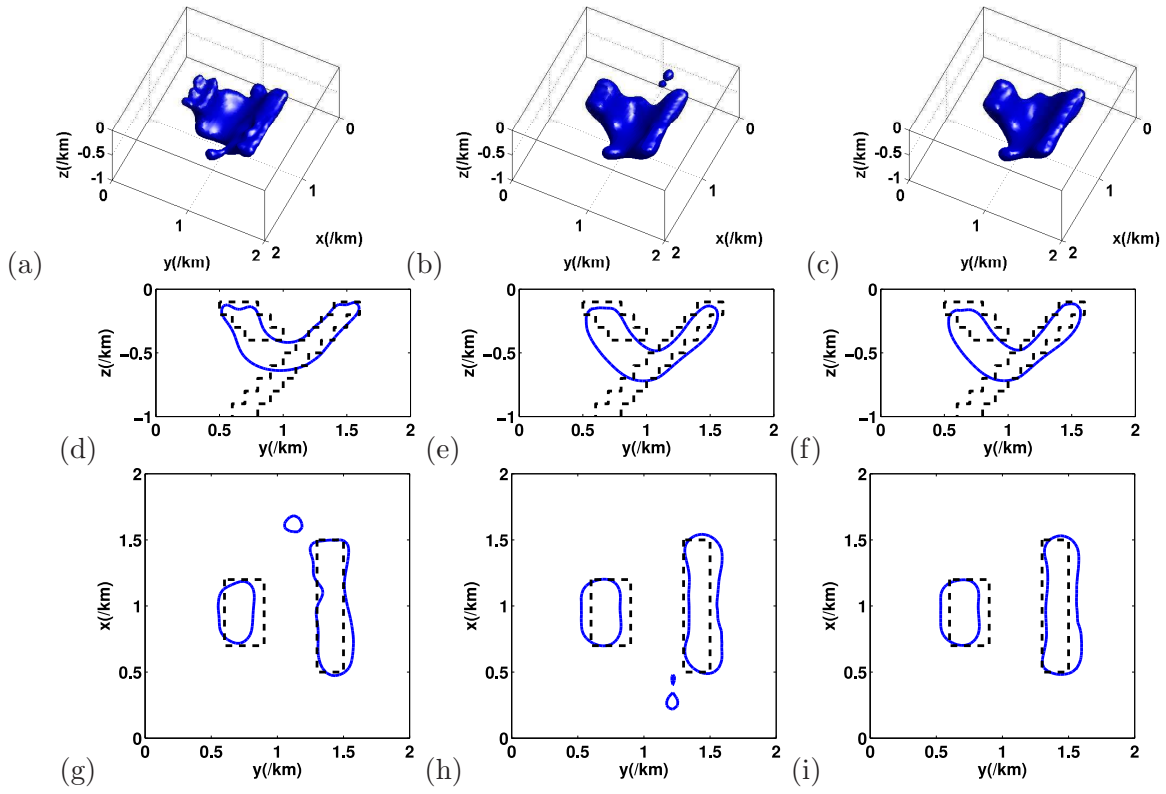


Figure 18: Two dykes. Shapes of numerical solutions at the 2000th iteration for  $\rho = 1.0\text{g/cm}^3$  with a one-sphere initial guess for different index sets. (a):  $M = \{xy, \Delta\}$ ; (b):  $M = \{zz\}$ ; and (c):  $M = \{xy, \Delta, zz\}$ . (d-f): cross sections of the numerical solutions in (a-c) at  $x = 1\text{km}$ . (g-i): cross sections of the numerical solutions in (a-c) at  $z = -0.25\text{km}$ . Dashed lines indicate the true positions of the target.

## LIST OF TABLES

- 1 Running time for computing Frechet derivatives, with the index set  $\mathcal{M} = \{xy, \Delta\}$ , in one iteration by two approaches in all numerical examples.

	Direct matrix-vector multiplication	Low-rank-matrix decomposition algorithm
Two cubes	0.95s	0.05s
Three cuboids	2.36s	0.12s
Two dykes	11.06s	0.32s
Five cuboids	9.53s	0.38s

Table 1: Running time for computing Frechet derivatives, with the index set  $\mathcal{M} = \{xy, \Delta\}$ , in one iteration by two approaches in all numerical examples.